



## RESEARCH ARTICLE

10.1029/2022GC010741

In-Situ and Triple Oxygen Isotope Characterization of  
Seafloor Drilled Cherts: Marine Diagenesis and Its Bearing on  
Seawater Reconstructions

## Key Points:

- Mesozoic and Cenozoic seafloor-drilled cherts were measured for triple O-isotope and in situ secondary ion mass spectrometry  $\delta^{18}\text{O}$ - $^{16}\text{OH}/^{16}\text{O}$  values
- In situ measurements display up to 6‰ range in the  $\delta^{18}\text{O}$  values of seafloor-drilled cherts
- The  $\delta^{18}\text{O}$ - $\Delta^{17}\text{O}$  values of cherts plot near and under the silica-seawater equilibrium curve (20°C–40°C). Together with the in-situ variability, these data are best explained by a combination of original precipitation and recrystallization in sub-seafloor conditions

## Supporting Information:

Supporting Information may be found in the online version of this article.

## Correspondence to:

D. O. Zakharov,  
david.zakharov@wmich.edu

## Citation:

Zakharov, D. O., Marin-Carbonne, J., Pack, A., Di Rocco, T., Robyr, M., & Vennemann, T. (2023).

In-situ and triple oxygen isotope characterization of seafloor drilled cherts: Marine diagenesis and its bearing on seawater reconstructions. *Geochemistry, Geophysics, Geosystems*, 24, e2022GC010741. <https://doi.org/10.1029/2022GC010741>

Received 18 OCT 2022

Accepted 25 JAN 2023

## Author Contributions:

**Conceptualization:** David O. Zakharov, Johanna Marin-Carbonne, Andreas Pack, Tommaso Di Rocco

**Data curation:** David O. Zakharov, Johanna Marin-Carbonne, Andreas Pack, Martin Robyr, Torsten Vennemann

David O. Zakharov<sup>1,2</sup> , Johanna Marin-Carbonne<sup>2</sup>, Andreas Pack<sup>3</sup> , Tommaso Di Rocco<sup>3</sup>, Martin Robyr<sup>2</sup> , and Torsten Vennemann<sup>2</sup>

<sup>1</sup>Department of Geological and Environmental Sciences, Western Michigan University, Kalamazoo, MI, USA, <sup>2</sup>Faculty of Geosciences and Environment, University of Lausanne, Lausanne, Switzerland, <sup>3</sup>Geowissenschaftliches Zentrum, Georg-August-Universität Göttingen, Göttingen, Germany

**Abstract** Cherts are used to reconstruct the evolution of seawater  $\delta^{18}\text{O}$  and temperature over geological time. However, given the influence of marine diagenesis, reconstructing seawater from the isotope composition of cherts is not straightforward, resulting in ambiguity of interpretation. Here, we present a detailed isotope and petrographic investigation of deep-sea drilled 135–40 Ma cherts with focus on the effects of marine diagenesis. We combined triple O-isotope data with in-situ  $\delta^{18}\text{O}$ - $^{16}\text{OH}/^{16}\text{O}$  measurements using secondary ion mass spectrometry (SIMS). We also provide electron microprobe maps, traditional  $\delta^{18}\text{O}$  measurements from petrographically diverse domains, and  $\delta\text{D}$  and  $\text{H}_2\text{O}$  wt.% values. The bulk  $\delta^{18}\text{O}$  values range between 29‰ and 38‰ in our collection, while SIMS  $\delta^{18}\text{O}$  data reveal significant intra-sample heterogeneities up to 6‰ related to distinct petrographic features (e.g., filled radiolarian tests) and to micrometer-scale variations in silica forms. Further, the  $\delta^{18}\text{O}$ — $\Delta^{17}\text{O}$  values of these seafloor-drilled cherts plot near and under equilibrium curve. Both triple-O and SIMS  $\delta^{18}\text{O}$  results reflect diagenesis in presence of marine pore waters at temperatures higher than ambient seawater, which is especially appreciable in cherts deposited on young oceanic crust. Despite the relatively constant  $\delta^{18}\text{O}$  seawater values over last 135 Ma, the marine silica spanning between 0 and 135 Ma occupies a wide compositional space in the  $\delta^{18}\text{O}$ — $\Delta^{17}\text{O}$  rather than an equilibrium curve. The  $\delta^{18}\text{O}$  values of cherts from modern-seafloor positively correlate with the oceanic crustal age at the time of deposition, hinting at the importance of the heat flux in the diagenetic recrystallization of marine silica.

**Plain Language Summary** Chemical sediments extracted from seafloor represent an archive of ocean temperatures and solutes. Chemical resilience of siliceous sediments with composition of >90 wt.%  $\text{SiO}_2$  presents a promising avenue to constrain temperature of ancient oceans from distant geological epochs. However, such rocks termed cherts undergo complex recrystallization during compaction and lithification below the seafloor, preventing direct measurements of ocean temperatures. To isolate the effect of diagenesis, we carefully investigated several Mesozoic and Cenozoic seafloor-drilled cherts. We used oxygen isotope ratios as a common proxy for temperature to test for the effects of recrystallization of these cherts that were buried at depths between 80 and 960 m. We combined two state-of-the-art types of isotope measurements: (a) non-destructive in-situ measurements from microscopic domains and (b) bulk high-precision triple O-isotope ratios. We observe complex mineralogical and isotope compositions on the scale of 10–100  $\mu\text{m}$ . The triple O-isotope ratios depict the combined effects of original precipitation from seawater column and the thermal regime of recrystallization in subseafloor conditions. The compiled O-isotope ratios of silica extracted from seafloor correlates with the age of oceanic crust. Since the age of oceanic crust and the heat flux are related, these observations hint at the importance of the sediment geothermal evolution during diagenesis.

## 1. Introduction

The oxygen isotope composition ( $\delta^{18}\text{O}$ ) of marine carbonates is a well-established proxy for the Cenozoic climate (Lisiecki & Raymo, 2005; Zachos et al., 2001). With small corrections for diagenesis and changes in the  $\delta^{18}\text{O}$  of seawater, the  $\delta^{18}\text{O}$  of marine carbonates are used to quantitatively estimate ocean temperatures across the last 65 Ma with a sensitivity of about 1°C and high temporal accuracy (e.g., Raymo et al., 2018). The principle of isotope thermometry is based on the temperature-dependent fractionation of oxygen isotopes between co-existing marine carbonates and seawater (Epstein et al., 1951). Consequently, oxygen isotope thermometry bears a

© 2023 The Authors.

This is an open access article under the terms of the [Creative Commons Attribution-NonCommercial License](#), which permits use, distribution and reproduction in any medium, provided the original work is properly cited and is not used for commercial purposes.

**Formal analysis:** David O. Zakharov, Andreas Pack, Tommaso Di Rocco, Martin Robyr, Torsten Vennemann  
**Funding acquisition:** Johanna Marin-Carbonne  
**Investigation:** David O. Zakharov, Johanna Marin-Carbonne, Andreas Pack, Tommaso Di Rocco  
**Methodology:** David O. Zakharov, Johanna Marin-Carbonne, Andreas Pack, Tommaso Di Rocco, Martin Robyr, Torsten Vennemann  
**Project Administration:** Johanna Marin-Carbonne  
**Resources:** Johanna Marin-Carbonne  
**Software:** David O. Zakharov  
**Supervision:** Johanna Marin-Carbonne  
**Validation:** David O. Zakharov  
**Visualization:** David O. Zakharov, Johanna Marin-Carbonne, Martin Robyr, Torsten Vennemann  
**Writing – original draft:** David O. Zakharov, Johanna Marin-Carbonne, Andreas Pack, Tommaso Di Rocco, Martin Robyr, Torsten Vennemann  
**Writing – review & editing:** David O. Zakharov, Johanna Marin-Carbonne, Andreas Pack, Tommaso Di Rocco, Martin Robyr, Torsten Vennemann

potential to reveal the state of climate during the early geological history, that is, the Archean eon (>2,500 Ma) for which surface temperatures remain poorly constrained and are most controversial (see Catling & Zahnle, 2020). However, considering the  $\delta^{18}\text{O}$  values of marine precipitates across the entire geological time scale, carbonates are unlikely to represent a trustworthy archive of seawater temperatures owing to their proneness to recrystallization, dissolution and precipitation in crustal conditions (e.g., Bernoulli & Weissert, 2021; Veizer et al., 1989).

Compared to carbonates, marine cherts are less soluble and are less prone to recrystallization once they experienced post-depositional burial diagenesis (Kolodny & Epstein, 1976). Initially, cherts originate due to precipitation of fully amorphous silica (opal-A) from water or within sediment, and subsequent maturation to opal-CT and to microcrystalline quartz. Cherts are >90 vol.% microcrystalline quartz (hereinafter, microquartz). Common impurities include carbonates, clays, volcanic ash and detrital material. In modern-day oceans and lakes, precipitation of amorphous silica is biologically mediated via growth of silicious sponges, diatom frustules and radiolarian skeletons, while final diagenetic crystallization of microquartz occurs below the seafloor. The  $\delta^{18}\text{O}$  of amorphous silica is a calibrated paleoclimate proxy, used in marine (e.g., Shemesh et al., 1992) and lacustrine settings (e.g., Leng & Barker, 2006), largely for the last <3 Ma. A typical  $\delta^{18}\text{O}$  value of marine biogenic silica is about 42‰–44‰ higher than co-existing seawater, corresponding to a water temperature of about  $0^\circ\text{C} \pm 2^\circ\text{C}$  (e.g., Shemesh et al., 1992).

In contrast, older cherts represent products of post-depositional burial marine diagenesis composed of microquartz that recrystallizes on the timescales of ~10 Ma after original deposition (Kolodny & Epstein, 1976). Consequently, cherts may only indirectly constrain the ancient ocean temperatures because their  $\delta^{18}\text{O}$  values are affected by seafloor diagenesis. Multiple studies documented that even recent marine siliceous sediments underwent complex post-depositional recrystallization associated with a transition of amorphous silica to opal-CT to microquartz under the influence of marine pore water fluids and elevated temperature within the sediment column (Behl et al., 1994; Knauth & Epstein, 1975; Kolodny & Epstein, 1976; Murata et al., 1977; Yanchilina et al., 2020). Studies of cherts sampled from modern seafloor and terrestrial outcrops show that the  $\delta^{18}\text{O}$  values are lower by over 10‰ compared to the initial values due to the transition of opaline silica to microcrystalline quartz (Behl & Smith, 1992; Behl et al., 1994; Ibarra et al., 2022; Kolodny & Epstein, 1976; Matheny & Knauth, 1993; Murata et al., 1977; Yanchilina et al., 2020). These diagenetic changes in  $\delta^{18}\text{O}$  during chert maturation obscure the original  $\delta^{18}\text{O}$ , hindering our understanding of seawater (temperature and O-isotope composition) evolution in the distant past.

The  $\delta^{18}\text{O}$  of older cherts, for example, from the Archean, are on average 10‰–15‰ lower than those of the Phanerozoic cherts (e.g., Knauth & Epstein, 1976; Perry & Tan, 1972). Despite the strong influence of metamorphism and diagenesis, face-to-face comparison of Archean and Phanerozoic cherts is frequently used to imply that Archean seawater temperatures were close to  $70^\circ\text{C}$ – $100^\circ\text{C}$  (e.g., Knauth & Lowe, 1978). Alternatively, Archean seawater itself was 10‰–15‰ lower compared to modern seawater entailing an evolution of tectonic mechanisms that control the seawater O-isotope budget (see Jaffrés et al., 2007; Kasting et al., 2006). The recent triple O-isotope data of Sengupta and Pack (2018) and Sengupta et al. (2020) suggested that Archean oceans were neither hot nor was the Archean seawater  $\delta^{18}\text{O}$  much lower than today. Meanwhile, Herwartz et al. (2021) demonstrated that enhanced carbonatization and silicification may have shifted Archean seawater by about ~5‰ toward lower  $\delta^{18}\text{O}$  values, while not changing the  $\Delta^{17}\text{O}$  toward much higher values, such as suggested by Sengupta and Pack (2018). A recent interpretation of the chert record highlights the effect of secular cooling of the Earth that in turn controls the temperature of diagenesis within the sediment column. Consequently, the observed shift in  $\delta^{18}\text{O}$  values across the Archean could be in part explained by the thermal evolution of the planet (Tatzel et al., 2022). In the same vein, present paper investigates the thermal conditions of the seafloor sediment.

Each of these interpretations are not mutually exclusive and clearly have great implications for the climate and the overall evolution of Earth's hydrosphere. Consequently, the ancient chert record has been at the center of a long-standing, unresolved debate concerning seawater temperatures and  $\delta^{18}\text{O}$  values (Galili et al., 2019; Guo et al., 2022; Jaffrés et al., 2007; Kanzaki & Bindeman, 2022; Kasting et al., 2006; McGunnigle et al., 2022; Muehlenbachs, 1998).

In this paper, we revise the understanding of marine diagenesis and its bearing on the O isotope composition of cherts. We utilize recent analytical developments in studies of cherts including the high-precision triple O-isotope analyses (Levin et al., 2014; Pack & Herwartz, 2014) and secondary ion mass spectrometry (SIMS; e.g., Heck et al., 2011; Marin et al., 2010; Marin-Carbonne et al., 2013; Robert & Chaussidon, 2006).

These methods provide a means to unravel the post-depositional alteration of the isotope compositions (e.g., Zakharov, Marin-Carbonne, et al., 2021). While triple O-isotope measurements require 1–2 mg of bulk sample for high precision  $\delta^{17}\text{O}$  and  $\delta^{18}\text{O}$  values ( $2\text{SD} < 0.1\text{‰}$ ), the SIMS measurements is in-situ from 10 to 20  $\mu\text{m}$  diameter spots with a precision on the order of  $0.1\text{‰}$ – $0.3\text{‰}$  for  $\delta^{18}\text{O}$  and  $0.5\text{‰}$ – $1\text{‰}$  for  $\delta^{17}\text{O}$ . While bulk  $\delta^{18}\text{O}$  and  $\Delta^{17}\text{O}$  measurements are precise, the SIMS measurements allow to demonstrate microscale variations in  $\delta^{18}\text{O}$ . The triple O-approach has recently been applied to a plethora of Precambrian and Phanerozoic formations (Hayles et al., 2019; Ibarra et al., 2022; Liljestr nd et al., 2020; Lowe et al., 2020; Sengupta et al., 2020; Wostbrock & Sharp, 2021; Zakharov, Marin-Carbonne, et al., 2021) with the goal to reconstruct the  $\delta^{18}\text{O}$  evolution of seawater. The SIMS  $\delta^{18}\text{O}$  measurements were also widely used to investigate Precambrian cherts and their diagenetic history (Cammack et al., 2018; Heck et al., 2011; Marin et al., 2010; Marin-Carbonne et al., 2013; Robert & Chaussidon, 2006; Stefurak et al., 2015). These studies revealed that microscale and triple O-isotope variability of cherts reflect the combined effect of original precipitation, diagenesis, metamorphism and mixed silica sources in the Precambrian oceans, that cannot be avoided in reconstructions of ancient seawater (e.g., Marin-Carbonne et al., 2013; Sengupta et al., 2020; Zakharov, Marin-Carbonne, et al., 2021).

This study specifically focuses on recent (Cretaceous to late Eocene; 135–40 Ma) cherts that underwent diagenesis in a deep-sea marine environment but were never subaerially exposed, that is, drilled from the seafloor. We combine the triple O-isotope and in situ  $\delta^{18}\text{O}$  SIMS measurements on the same samples to resolve the environmental influence recorded by seafloor cherts. These cherts were (partially or completely) transformed to microquartz in subseafloor environments and were drilled during the expeditions of the Ocean Drilling Program (see Table 1). In addition, we present the same set of measurements on a chert sampled from the subaerial late Cretaceous Mishash Formation in Israel. Cherts of the Mishash formation are found within the sequence of chalks, phosphorites and organic matter-rich rocks that likely formed in a series of shallow semi-closed basins (Kolodny, 1969). The sample studied here originally comes from the collection of Yehoshoua Kolodny and more information about these cherts can be found in previous publications (Kolodny, 1969; Kolodny et al., 1980). The O-isotope ratios of these samples were originally presented by Kolodny and Epstein (1976), where they were measured by a conventional bulk fluorination technique (Taylor & Epstein, 1962). We apply detailed O-isotope measurements of these cherts at the scale of several  $\mu\text{m}$  to mm. Further, since chert contains water in form of hydrated opal ( $\text{SiO}_2 \cdot \text{H}_2\text{O}$ ) as well as silanol groups (Si-O-H) in quartz, we adopt a novel strategy to document isotope variations between different variety of silica by (a) measuring the  $^{16}\text{OH}/^{16}\text{O}$  ratios concurrently with the  $\delta^{18}\text{O}$  by SIMS (b) electron microprobe mapping of analyzed domains. Such an approach is warranted because there is a limited number of in situ SIMS studies that address the analytical protocols for measuring hydrous silica species.

## 2. Sample Collection

The samples (see Figure 1) were drilled by the Ocean Drilling Program, thus, the core stratigraphy and lithology can be found in the scientific reports using the sample number provided (<http://www-odp.tamu.edu/publications/>). These cores (see detailed description in Table 1) contain cherts ranging in age from 135 to 40 Ma. Previous isotope characterization of these samples can be found in Kolodny and Epstein (1976) and Kolodny and Chaussidon (2004). These samples contain various petrographic varieties of silica, namely, microcrystalline quartz (commonly referred to as microquartz), chalcedony and opal. Most samples are composed of >90 wt.% microcrystalline quartz with minor opal, carbonates, and clays present. Porcellanite is used to describe an early diagenetic variety of highly opaline and porous silicious rock with dull luster (e.g., Kolodny, 1969). In one drill core sample, porcellanite notably occurs as a rim around red-brown chert (Figure 1). In addition, we provide measurements of one sample of subaerially exposed chert KF304 from the Mishash Formation, Israel (Kolodny et al., 1980, 2005). It is used here to exemplify the differences between the subaerially exposed cherts, and the seafloor drilled samples.

Finally, we include a hydrous sample of opal-CT. It is represented by the tridymite-dominated variety of opal with ~5 wt.%  $\text{H}_2\text{O}$  (see X-ray diffraction, Raman spectroscopy and electron microprobe determinations in Figures S1–S4 in Supporting Information S1) to calibrate the SIMS measurements for the potential analytical artifacts. The opal-CT sample comes from the collection of Cantonal Geological Museum (Mus e cantonal de g eologie, Lausanne), originally sampled at the locality Pont-du-Ch ateau in France and is termed “MGL opal-CT” here.

**Table 1**  
*Description of Seafloor-Drilled Cherts and One Subaerially Exposed Chert Used in This Study*

| Chert                                | Age, Ma                        | Depth, meters below seafloor | Location (decimal °)   | Core lithology   | Sample description  |
|--------------------------------------|--------------------------------|------------------------------|--|--|---|
| 195-20-4cc <sup>a,c</sup>            | 135                            | 275                          | 32.7733°N, 146.9783°E<br>Abyssal floor east of Izu-Bonin Trench, Pacific Ocean | Chert and limestone  | Red brown chert (microquartz) fragments with rims of porcellanite. Preserved Radiolaria                       |
| 167-73-2-90-92 <sup>b,d</sup>        | 130                            | 960                          | 7.068333°N, 176.825°E<br>Magellan Rise, Central Pacific Ocean                  | Limestone and chert  | Pink chert (microquartz + opal) with carbonate lenses. Abundant well-preserved Radiolaria                     |
| KF304 Mishash Formation <sup>e</sup> | 84–72; Late Campanian          | NA subaerially exposed       | 30.2°N, 35.0°E Arabah valley, Israel   | Brown chert and porcellanite                                     | Massive, banded chert (microquartz)   |
| 52-6-10cc <sup>a,f</sup>             | 72–66; Early Cretaceous        | 67                           | 27.7717°N, 147.1300°E<br>Abyssal floor east of Japan, Pacific Ocean            | Dark brown silty clay with volcanic ash and radiolarian remnants | Yellowish porcellanite  |
| 13A-3-1 <sup>a,g</sup>               | 48–41; Lutetian, Middle Eocene | 180                          | 6.0400°N, 18.2285°W<br>North Atlantic Ocean                                    | Radiolarian oozes with chert member                              | Gray-white porcellanite   |
| 167-17-33-147-149 <sup>b,d</sup>     | 43                             | 605                          | 7.068333°N, 176.825°E<br>Magellan Rise, Central Pacific Ocean                  | Chert, nannofossil chalk and limestone                           | Pinkish gray chert (microquartz-dominated), rich in carbonate. Rare carbonate remnants of foraminifera.       |
| 167-17-33-127-129 <sup>b,d</sup>     | 42.5                           | 605                          | 7.068333°N, 176.825°E<br>Magellan Rise, Central Pacific Ocean                  | Chert, nannofossil chalk and limestone                           | Gray translucent chert (microquartz + opal) fragments with porcellanite rims. Silicified foraminifera present |
| 466-9-1-64-65 <sup>h</sup>           | ~40 Ma; Late Eocene            | 80                           | 33.191°N, 179.2557°E<br>Hess Rise, North Pacific                               | Cherty nannofossil ooze  | Waxy gray chert (abundant opal + microquartz). Heavily recrystallized microfossils                            |

Note. References for previous  $\delta^{18}\text{O}$  determinations.

<sup>a</sup>Kolodny and Epstein (1976). <sup>b</sup>Kolodny and Chaussidon (2004). *References for the lithological context and drilling site information:* <sup>c</sup><https://doi.org/10.2973/dsdp.proc.20.103.1973>. <sup>d</sup><https://doi.org/10.2973/dsdp.proc.17.105.1973>. <sup>e</sup>Kolodny et al. (1980). <sup>f</sup><https://doi.org/10.2973/dsdp.proc.6.110.1971>. <sup>g</sup><https://doi.org/10.2973/dsdp.proc.3.103.1970>. <sup>h</sup><https://doi.org/10.2973/dsdp.proc.62.105.1981>.

### 3. Methods

The combination of analytical approaches is detailed in this section in the order they were applied to the samples:

1. Bulk 1–2 mg sample  $\delta^{18}\text{O}$  laser fluorination measurements from multiple petrographically different domains (see Figure 1) and subsequent triple O-isotope measurements
2. Chert samples and MGL opal-CT were measured for  $\delta\text{D}$  and  $\text{H}_2\text{O}$  content. These measurements allow to gauge the relationship between the  $^{16}\text{OH}/^{16}\text{O}$  ratio measured by SIMS and the actual  $\text{H}_2\text{O}$  concentration.
3. Microscale in situ  $\delta^{18}\text{O}$  and  $^{16}\text{OH}/^{16}\text{O}$  measurements by SIMS from chosen domains using a 10–15  $\mu\text{m}$  ion beam
4. Electron microprobe characterization of the analyzed domains

The following definitions are used to report the O-isotope results:

$$\delta^{18}\text{O} = 10^3 \cdot \ln(\delta^{18}\text{O}/1000 + 1) \text{ and } \delta^{17}\text{O} = 10^3 \cdot \ln(\delta^{17}\text{O}/1000 + 1),$$

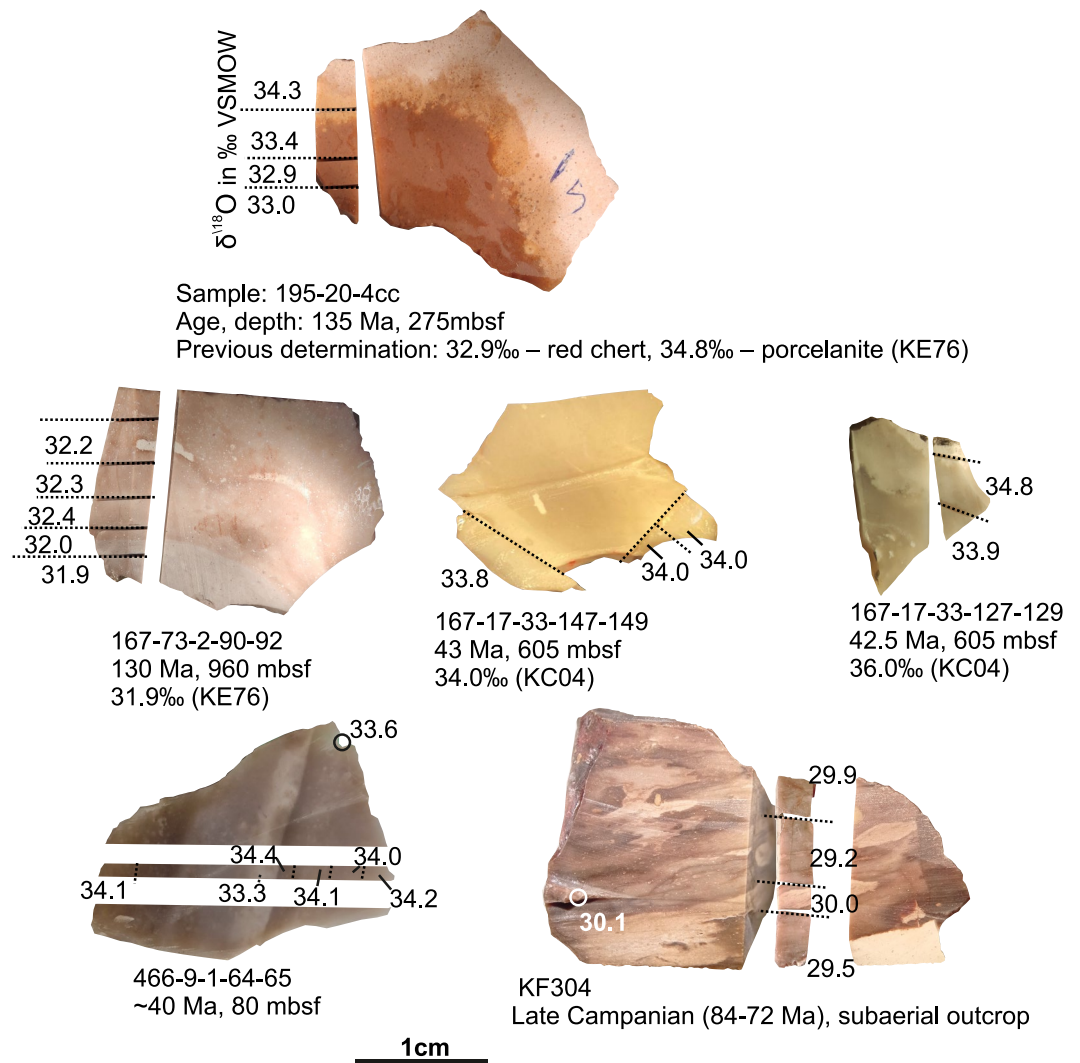


**Figure 1.** The collection of cherts used in this study for detailed investigation by laser fluorination  $\delta^{18}\text{O}$ ,  $\Delta^{17}\text{O}$  and in situ secondary ion mass spectrometry measurements. The seafloor samples are titled with the drilling program core numbers (Kolodny & Epstein, 1976), while the chert KF304 is from the Cretaceous Mishash formation (Kolodny et al., 2005). Previous  $\delta^{18}\text{O}$  determinations are from (Kolodny & Epstein, 1976) and (Kolodny & Chaussidon, 2004) labeled KE76 and KC04, respectively. Each sample was cut with a wire saw and measured by bulk laser fluorination. The wire saw cuts are shown with dashed lines, where not apparent. The corresponding  $\delta^{18}\text{O}$  values are printed next to the measured fragment.

where  $\delta^{17}\text{O}$  and  $\delta^{18}\text{O}$  are the conventionally expressed  $\delta$ -notations on the VSMOW scale. The triple O-isotope composition is expressed through the relationship:

$$\Delta^{17}\text{O} = \delta^{17}\text{O} - 0.528 \cdot \delta^{18}\text{O}.$$

### 3.1. Bulk Laser Fluorination for Determination of $\delta^{18}\text{O}$ and $\Delta^{17}\text{O}$ Values

The triple O-isotope values of bulk chert samples were determined by laser-assisted fluorination mass spectrometry at the Institute of Earth Surface Dynamics, University of Lausanne and at the Georg-August University of Göttingen. The laboratory at the University of Lausanne was used exclusively for high-throughput  $\delta^{18}\text{O}$  measurements in petrographically diverse fragments within each sample (see Figure 1), while a subset of fragments was measured at the Georg-August University of Göttingen for high-precision triple-O isotope measurements. Each chert fragment was cut with a wire saw and hand-picked under a binocular microscope. We used weak HCl to remove calcite from carbonate-rich fragments present in sample 167-73-2-90-92 prior to measurements.

Samples were loaded in a platinum sample holder as whole rock fragments, ranging in quantities between 1 and 2 mg. At the University of Lausanne, each sample was heated in an oven to 110°C before loading the platinum tray in the sample chamber and subsequent evacuation to a high vacuum. After maintaining the samples for several hours at high vacuum ( $P \approx 10^{-6}$  mbar), each sample was pre-fluorinated in presence of ~50 mbar  $F_2$  gas overnight (12–14 hr) to get rid of excess moisture and hydration water. Overnight pre-fluorination also consumes highly reactive clays and hydroxyl-bounded water in opaline silica present in cherts (Dodd & Sharp, 2010). A subset of measurements was conducted to eliminate the effect of hydration water in opaline silica by increasing the time of exposure to  $F_2$ . Extraction of  $O_2$  gas was mediated via heating with  $CO_2$  laser in presence of  $F_2$  gas ( $P \approx 100$  mbar). The extracted  $O_2$  gas was transferred through a series of cryogenic traps and collected on molecular sieve 5A. The collected oxygen was introduced into the dual inlet of a MAT 253 mass spectrometer, where every measurement consisted of 8 cycles of comparisons between the reference and analyte  $O_2$ . For monitoring the accuracy of measurements and for day-to-day corrections, the University of Lausanne in-house quartz standard LS1 ( $\delta^{18}O = 17.9\text{‰}$  VSMOW) was routinely loaded into the same chamber with the samples and measured within the session. Typical reproducibility of LS1 standard was 0.2‰.

The triple-O isotope measurements at Georg August University of Göttingen is described in detail previously (Pack et al., 2016). The procedure is overall similar to the laser fluorination measurement described above. We used  $BrF_3$  as a reagent to extract  $O_2$ . The resulted  $O_2$  sample was purified by a series of cryogenic traps and subsequently trapped onto molecular sieve. Released from the molecular sieve, the sample  $O_2$  gas was transported through a gas chromatograph via a  $10 \text{ mL min}^{-1}$  He carrier gas for further purification from  $NF_3$  and other gases (e.g.,  $N_2$ ). The gas was introduced to a MAT253 mass spectrometer via dual inlet mode. The uncertainty (obtained from the 1 S.D. external reproducibility of the olivine and garnet standards) is  $\pm 0.3\text{‰}$  or better for  $\delta^{18}O$  and  $\pm 0.005\text{‰}$  for  $\Delta^{17}O$ . There is no silicate reference material available with certified  $\delta^{17}O$  (relative to VSMOW). Therefore, we use an average  $\Delta^{17}O$  of studies by Pack et al. (2016), Sharp et al. (2016), and Wostbrock et al. (2020) of  $-0.051\text{‰}$  for San Carlos olivine as calibration anchor point (see also Miller et al., 2020).

### 3.2. Measurements of Hydrogen Isotope Composition ( $\delta D$ ) and $H_2O$ Content

The chert samples the MGL opal-CT were measured for hydrogen isotopes ( $\delta D$ ) and  $H_2O$  wt.% using a high temperature thermal conversion elemental analyzer (TC/EA) connected to the MAT 253, where gases from samples and standards are transported with He carrier gas from EA to the inlet of the mass spectrometer (see Bauer & Vennemann, 2014). Samples and standards were wrapped in silver foil capsules and dried in an oven at 110°C and in a vacuum desiccator overnight. The capsules were then loaded directly into a zero-blank autosampler, where they were purged with He carrier gas. In the TC/EA's furnace lined with a glassy carbon column, samples underwent pyrolysis at 1450°C, and all of the  $H_2O$  in the minerals was pyrolyzed to  $H_2$  and CO gas. Extracted gas was carried by He into a gas chromatograph and further introduced into the mass spectrometer via a CONFLO III. Mica standards, USGS57 and USGS58 ( $\delta D = -91\text{‰}$  and  $-28\text{‰}$ , respectively; Qi et al., 2017) were included in each analytical session to monitor the accuracy of analysis and to normalize data to VSMOW scale. Peak areas of the  $H_2$  in the mass spectrometer for standards and samples were used for determining the  $H_2O$  wt.%. The mass of samples ranged between 2 and 7 mg.

### 3.3. In Situ $\delta^{18}O$ and $^{16}OH/^{16}O$ Measurements by SIMS

The  $\delta^{18}O$  values of cherts were determined in situ using the Cameca IMS 1270 secondary ion mass spectrometer equipped with a cesium ion source installed at the CRPG-CNRS in Nancy, France. A subset of measurements on the same samples was measured using the Cameca IMS 1280 HR at the SwissSIMS, University of Lausanne.

The chert fragments were mounted in indium together with quartz standards UNILQ1 ( $\delta^{18}O = 9.8\text{‰}$  VSMOW) and LS1. Fragments of MGL opal-CT were also mounted to quantify the matrix effects potentially encountered in measuring cherts. Indium was used as the mounting medium to minimize outgassing in the sample chamber. Prior to mounting in indium, the standard grains were mounted in epoxy and polished. Fragments of cherts were mounted together with the standards. The chert fragments were first used to make thin sections. Resulted thin sections were studied in transmitted light first, then sliced into smaller fragments (20–30 mm<sup>2</sup>) using wire saw. Prior to analyses, the indium mounts were carefully washed, dried in an oven (60°C), outgassed under

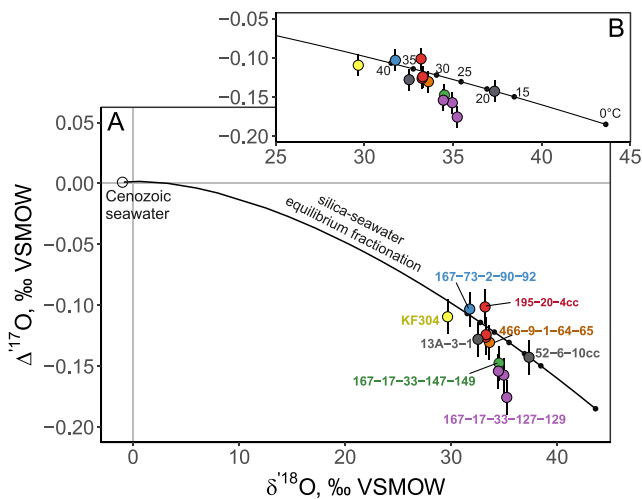


**Figure 2.** (a) Triple O-isotope values of cherts measured in our collection. Each chert is labeled, and duplicates of the same samples are color-coded with the same color. The inset shows the same samples enlarged. The solid black line is silica-seawater equilibrium fractionation (Wostbrock & Sharp, 2021). (b) The inset shows an enlarged version of the same diagram with temperature of silica-seawater equilibrium labeled from 0°C to 40°C.

vacuum and coated with a 35-nm thick layer of gold. During the analyses, the liquid nitrogen trap was used to obtain the best possible vacuum. The analyses employed a 10 kV Cs<sup>+</sup> primary ion beam with a ~2 nA current focused on a ~10 μm diameter spot. Pre-sputtering of targeted areas during 45 s was applied with a 10 μm raster before each measurement. The secondary ions were extracted using negative 10 kV potential applied to the sample holder. The <sup>18</sup>O/<sup>16</sup>O ratios were measured using the mass resolving power of ~2,400 in a multi-collection mode using two off-axis L2 and H1 Faraday cup (FC) detectors. The obtained ion intensities of <sup>16</sup>O and <sup>18</sup>O were around 1.2–1.9 × 10<sup>9</sup> and 2.1–4.2 × 10<sup>6</sup> counts per second, respectively. We also monitored the presence of water-containing domains (e.g., opaline silica) in the samples using the <sup>16</sup>OH/<sup>16</sup>O ratio. Concurrently with the <sup>18</sup>O/<sup>16</sup>O ratio, the <sup>16</sup>OH<sup>-</sup> ion was measured on the axial FC2 detector using the mass resolving power of 5,000 to separate the interference from <sup>17</sup>O<sup>-</sup>. Each measurement consisted of 30 cycles with counting time of 5 s per cycle. Several measurements of the UNILQ1 standards were made in the beginning and the end of the session to monitor stability and accuracy of the analyses. Blocks of 4–5 unknowns were bracketed by 2–3 measurements of the UNILQ1 standard. We also made several measurements of LS1 quartz grains to monitor the linearity of instrumental mass fractionation (IMF).

The instrumental uncertainty of δ<sup>18</sup>O measurements is typically around 0.2‰ (2 standard errors). The IMF is expressed as δ<sup>18</sup>O<sub>measured</sub> – δ<sup>18</sup>O<sub>VSMOW</sub>, where δ<sup>18</sup>O is the linearized delta notation, that is, 1000·ln(1 + δ<sup>18</sup>O/1000).

The IMF was assessed using the UNILQ1 standard grains. The IMF value systematically varied several ‰ during each analytical session, which is related to analytical tuning of SIMS. The analytical error of <sup>16</sup>OH/<sup>16</sup>O signals is typically around 0.2%–3% relative to the mean.

### 3.4. Electron Microprobe Mapping of Analyzed Domains

Thin section fragments of cherts with SIMS spots were investigated with a reflected and transmitted polarized light microscope and photographed. Further, selected areas were analyzed using the JEOL JXA-8530F electron microprobe at the University of Lausanne. The fine-grained samples were scanned to create elemental maps using grid analysis and the following operating conditions: beam current 15 nA, 15 kV operating voltage, beam diameter 1 μm and 0.1 s count time for each element per pixel. Spot analyses of selected minerals were performed under same conditions, except the beam diameter was 3 μm and the count time was 60 s per element. The SiO<sub>2</sub> measurements were compared with pure quartz, since cherts were mounted together with the SIMS standard grains of UNILQ1 quartz.

## 4. Results

### 4.1. Laser Fluorination Measurements: Traditional δ<sup>18</sup>O and Triple O-Isotope (δ<sup>18</sup>O—Δ<sup>17</sup>O) Values

The δ<sup>18</sup>O values range between 29‰ and 38‰ for the collection of cherts used in this study. The δ<sup>18</sup>O of multiple individual fragments of the six samples were measured as shown in Figure 1. Variability across petrographic varieties of fragments within each sample does not exceed 1.3‰. These values agree well with the original determinations in Kolodny and Epstein (1976) within 0.1‰–1.3‰. The δ<sup>18</sup>O values determined during the triple O-isotope analyses at University of Göttingen vary <1‰ compared to the traditional δ<sup>18</sup>O measurements conducted at the University of Lausanne. The δ<sup>18</sup>O—Δ<sup>17</sup>O values of 8 cherts are shown in Figure 2 and are listed in Table 2.

The MGL opal-CT sample returned mean δ<sup>18</sup>O value of 28.0‰. To appreciate the effect of hydration water, MGL opal-CT was subjected to various pre-fluorination conditions. Overnight pre-fluorination at room temperature caused almost complete consumption of MGL opal-CT by reaction with F<sub>2</sub>. Step-wise pre-fluorination with several aliquots of 100 mbar F<sub>2</sub> recommended for hydrous diatom frustule analyses (Dodd & Sharp, 2010) did not give systematically different δ<sup>18</sup>O values from those measured in absence of pre-fluorination. However,

**Table 2**  
The Results of Triple O-Isotope Laser Fluorination and Thermal Conversion Elemental Analyzer (TC/EA) Measurements of Cherts

| Chert                             | $\delta^{18}\text{O}$ in multiple fragments (Figure 1) ‰<br>VSMOW (range; n) | $\delta^{17}\text{O}$ ‰<br>VSMOW | $\delta^{18}\text{O}$ ‰<br>VSMOW | $\delta^{17}\text{O}$ ‰<br>VSMOW | $\delta^{18}\text{O}$ ‰<br>VSMOW | $\Delta^{17}\text{O}$ ‰<br>VSMOW,<br>0.528 ref.<br>line | $\delta\text{D}$ by<br>TC/<br>EA ‰<br>VSMOW | $\text{H}_2\text{O}$<br>by<br>TC/<br>EA<br>(wt.<br>%) |
|-----------------------------------|--|----------------------------------|----------------------------------|----------------------------------|----------------------------------|---|---|---|
| 195-20-4cc                        | 33.4–34.9; n = 4   | 17.584                           | 33.812                           | 17.431                           | 33.253                           | −0.126  | −85.0                                       | 1.5   |
| 195-20-4cc-replicate1             |  | 17.606                           | 33.850                           | 17.453                           | 33.290                           | −0.124  |   |   |
| 195-20-4cc-replicate2             |  | 17.578                           | 33.751                           | 17.425                           | 33.194                           | −0.101  |   |   |
| 167-73-2-90-92                    | 32.4–32.9; n = 5   | 16.798                           | 32.255                           | 16.658                           | 31.746                           | −0.103  | −81.8                                       | 1.2   |
| KF304 Subaerial Mishash Formation | 29.7–30.5; n = 4   | 15.669                           | 30.098                           | 15.548                           | 29.654                           | −0.110  | −86.6                                       | 1.0   |
| 52-6-10cc                         | –  | 19.763                           | 38.041                           | 19.570                           | 37.335                           | −0.143  |   |   |
| 13A-3-1                           | –  | 17.190                           | 33.056                           | 17.044                           | 32.521                           | −0.127  | −92.0 <sup>a</sup>                          | 1.5 <sup>a</sup>                                      |
| 167-17-33-147-149                 | 34.4–34.6; n = 3   | 18.239                           | 35.114                           | 18.075                           | 34.512                           | −0.147  | −92.4 <sup>a</sup>                          | 1.0 <sup>a</sup>                                      |
| 167-17-33-127-129                 | 34.5 and 35.4; n = 2   | 18.199                           | 35.050                           | 18.035                           | 34.450                           | −0.154  | −92.4                                       | 1.3   |
| 167-17-33-127-129-replicate1      |  | 18.467                           | 35.573                           | 18.299                           | 34.955                           | −0.158  |   |   |
| 167-17-33-127-129-replicate2      |  | 18.599                           | 35.863                           | 18.428                           | 35.235                           | −0.176  |   |   |
| 466-9-1-64-65                     | 33.9–34.8; n = 6   | 17.770                           | 34.179                           | 17.614                           | 33.608                           | −0.131  | −96.9                                       | 1.2   |

<sup>a</sup>The  $\delta\text{D}$  and  $\text{H}_2\text{O}$  values are from Kolodny and Epstein (1976) (Table 1; samples 167-33-1(113–115) and 13A-1-1(75)A).

after about 8–10 doses of pre-fluorination (800–1,000 mbar  $\text{F}_2$  cumulatively), the values are less scattered and higher on average. The total range of values is between 26.8‰ and 29.5‰ yielding the mean and standard deviation of 28.0‰  $\pm$  0.9‰ ( $n = 10$ ), while samples exposed to >800 mbar  $\text{F}_2$  ( $n = 3$ ) yield values between 28.8‰ and 29.5‰. While methodology of pre-fluorination is not the focus of the paper, it seems that low doses of pre-fluorination (100–500 mbar  $\text{F}_2$ ) of the MGL opal-CT with ~5 wt.%  $\text{H}_2\text{O}$  result in a less pronounced effect compared to pre-fluorination of diatom frustules that contain up to 15 wt.%.

#### 4.2. SIMS $\delta^{18}\text{O}$ and $^{16}\text{OH}/^{16}\text{O}$ Measurements

The anhydrous grains of quartz (UNILQ1 and LS1) are used to calculate the difference between measured and true VSMOW value (i.e., the IMF) and to calibrate the unknowns to the  $\delta^{18}\text{O}$  VSMOW scale (see Figure S5 in Supporting Information S1). The IMF systematically ranged across the analytical sessions between −9‰ and −6‰. The typical reproducibility of UNILQ1 quartz within each session (May 2021, September 2021, and November 2021) was 0.3‰–0.6‰ (2SD;  $n = 229$ ). The net difference between LS1 and UNILQ1  $\delta^{18}\text{O}$  values remained the same within the analytical uncertainty (Figure S6 in Supporting Information S1). The MGL opal-CT with  $\delta^{18}\text{O} = 28.0‰$  VSMOW determined by fluorination has raw  $\delta^{18}\text{O}$  SIMS values of 26.5‰  $\pm$  2.0‰ (mean  $\pm$  2SD;  $n = 90$ ), resulting in IMF close to −2‰. Meanwhile, cherts display IMF values consistent the IMF measurements of the quartz standards. In other words, the UNILQ1-based correction applied to cherts results in their  $\delta^{18}\text{O}$  values being in agreement with the VSMOW-calibrated laser fluorination values. The difference between the IMF of MGL opal-CT and the IMF of the rest of the analytes (quartz standards and chert samples) is puzzling. It could be explained by the presence of high amounts of hydration water or/and structural differences that compose the MGL opal-CT. The range, median, mean and standard deviation for each chert sample on VSMOW scale are summarized in Table 3. The analytical parameters and raw  $\delta^{18}\text{O}$  values are reported in Data Set S1. The summary of bulk and SIMS measurements of MGL opal-CT is reported in the separate Table 4. The SIMS  $\delta^{18}\text{O}$  values are provided in raw form and relative to UNILQ1 (i.e., not calibrated to VSMOW).

The  $^{16}\text{OH}/^{16}\text{O}$  from all analytical sessions show consistently near-zero ratios for anhydrous standard grains (see Figure S5 in Supporting Information S1). All samples of cherts exhibit elevated  $^{16}\text{OH}/^{16}\text{O}$  values between 0.001 and 0.015. The raw  $\delta^{18}\text{O}$  plotted against  $^{16}\text{OH}/^{16}\text{O}$  (Figure 3) does not show a systematic relationship when all samples considered. However, porcellanite areas of chert (195-20-4cc) as well as MGL opal-CT have

**Table 3**  
The Summary of Bulk and Secondary Ion Mass Spectrometry (SIMS)  $\delta^{18}\text{O}$  and  $^{16}\text{OH}/^{16}\text{O}$  Measurements of Cherts

| Sample                  | $\delta^{18}\text{O}$ by laser fluorination (mean $\pm$ 2SD; in ‰ VSMOW) | No. points by SIMS | SIMS $\delta^{18}\text{O}$ mean $\pm$ 2D (‰, VSMOW) | SIMS $\delta^{18}\text{O}$ median, (‰, VSMOW) | SIMS $\delta^{18}\text{O}$ range, (‰, VSMOW) | SIMS $1,000 \times ^{16}\text{OH}/^{16}\text{O}$ mean (‰) | SIMS $1,000 \times ^{16}\text{OH}/^{16}\text{O}$ median (‰) | SIMS $1,000 \times ^{16}\text{OH}/^{16}\text{O}$ range (‰) |
|-------------------------|--|--------------------|---|---|--|---|---|--|
| 195-20-4cc <sup>a</sup> | 32.56 $\pm$ 1.51   | 133                | 34.1 $\pm$ 1.2                                      | 34.0  | 3.3  | 2.4   | 1.9   | 13.2   |
| 167-73-2-90-92          | 31.56 $\pm$ 0.48   | 103                | 32.4 $\pm$ 1.9                                      | 32.5  | 6.2  | 1.4   | 1.2   | 3.2  |
| 167-17-33-147-149       | 33.49 $\pm$ 0.54   | 85                 | 34.8 $\pm$ 0.9                                      | 34.7  | 2.1  | 1.3   | 1.3   | 0.8  |
| 167-17-33-127-129       | 34.23 $\pm$ 1.59   | 98                 | 35.2 $\pm$ 1.2                                      | 35.2  | 3.4  | 1.4   | 1.4   | 2.8  |
| 466-9-1-64-65           | 33.40 $\pm$ 0.72   | 120                | 33.9 $\pm$ 3.1                                      | 33.8  | 6.1  | 1.0   | 1.0   | 1.5  |
| KF304                   | 29.22 $\pm$ 0.63   | 42                 | 29.9 $\pm$ 1.4                                      | 29.9  | 2.5  | 1.4   | 1.4   | 0.9  |

<sup>a</sup>The  $\delta^{18}\text{O}$  values are based on measurements of  $^{16}\text{OH}/^{16}\text{O} < 3\text{‰}$  domains in the sample 195-20-4cc.

high  $^{16}\text{OH}/^{16}\text{O}$  that correlate negatively with raw  $\delta^{18}\text{O}$  (Figure 3). The  $\delta^{18}\text{O}$  values of these analytes do not agree with the laser fluorination measurements. These observations suggest that these samples contain a high fraction of hydration water which normally is removed by pre-fluorination and contributes its low  $\delta^{18}\text{O}$  value to the SIMS analyses. The negative correlation between  $\delta^{18}\text{O}$  and  $^{16}\text{OH}/^{16}\text{O}$  identifies the low  $\delta^{18}\text{O}$  hydration water commonly present in various amounts in opaline silica (Matheny & Knauth, 1993). The correlation between  $\delta^{18}\text{O}$  and  $^{16}\text{OH}/^{16}\text{O}$  appears to be insignificant at  $^{16}\text{OH}/^{16}\text{O}$  values below 0.003 (or  $1000 \cdot ^{16}\text{OH}/^{16}\text{O} < 3\text{‰}$ ). Consequently, we exclude analyzed domains with  $^{16}\text{OH}/^{16}\text{O} > 3\text{‰}$  from consideration as they represent a mixed signal between structural oxygen and oxygen derived from hydration water (Figure 3b). While  $^{16}\text{OH}/^{16}\text{O}$  ratio determined by SIMS is not a calibrated measurement, it is a direct indicator of  $\text{H}_2\text{O}$  content. Using the TC/EA-determined values, our data set gives us a rough calibration for  $^{16}\text{OH}/^{16}\text{O}$  versus  $\text{H}_2\text{O}$  concentration in cherts (Figure 3c). The  $^{16}\text{OH}/^{16}\text{O}$  ratios positively correlate ( $R^2 = 0.8$ ) with the  $\text{H}_2\text{O}$  content if we include measurements of nominally anhydrous quartz standards and the MGL opal-CT ( $\text{H}_2\text{O} = 5.2 \text{ wt.}\%$ ).

In our data set, the analyses with  $^{16}\text{OH}/^{16}\text{O}$  below  $\sim 3\text{‰}$  and with  $\text{SiO}_2$  above  $\sim 96 \text{ wt.}\%$  are unlikely to be subject to different IMF. We interpret that these samples are composed of microcrystalline mixtures of microquartz, chalcedony and low- $\text{H}_2\text{O}$  opal. Similar to previous studies (Marin-Carbonne et al., 2014; Oster et al., 2017), we find that most low-water cherts and quartz have the same IMF. Consequently, only VSMOW-normalized  $\delta^{18}\text{O}$  values are considered in Table 3. We show the distribution of  $\delta^{18}\text{O}$  values by SIMS in form of histograms (Figure 4a), with each distribution plotted against its value determined by bulk fluorination (Figure 4b). Across the range of values between 29‰ and 36‰ VSMOW, the SIMS mean and median  $\delta^{18}\text{O}$  values plot on 1:1 line, while individual samples have a range within 2.1‰–6.2‰ of their means (Figure 4b). While the mean SIMS  $\delta^{18}\text{O}$  measurements are in agreement with the bulk laser fluorination results, the SIMS  $\delta^{18}\text{O}$  measurements indicate that all cherts in our collection are more variable at a micrometer-scale than perceived by the bulk methods. The final propagated uncertainty of each individual  $\delta^{18}\text{O}$  measurement varies between 0.3‰ and 0.6‰ (2SD), and most of our samples have a variability beyond that (see Table 3).

### 4.3. $\delta\text{D}$ and Water Content Measurements

The  $\delta\text{D}$  and  $\text{H}_2\text{O}$  concentrations measured in cherts are reported in Table 2, including the values previously reported in Kolodny and Epstein (1976). The  $\delta\text{D}$  values range in a narrow interval between  $-97\text{‰}$  and  $-81\text{‰}$ , while the  $\text{H}_2\text{O}$  values are within 1.0–1.5 wt.%. The MGL opal-CT has  $\delta\text{D} = -80.0\text{‰}$  and  $\text{H}_2\text{O}$  concentration of 5.2 wt.%. The reproducibility of  $\delta\text{D}$  and  $\text{H}_2\text{O}$  results is within 2‰ and 0.1 wt.%, respectively. The  $\delta\text{D}$  values plotted against the triple O-isotope values are shown in Figure S7 in Supporting Information S1.

### 4.4. Electron Microprobe Analyses

Electron microprobe maps were used to create qualitative images of Si, Al, K, Ca, and Fe concentrations. The main variations are seen in Si and Al, and rarely in Ca, if carbonates are present. The Si and Al elemental maps are given in Figures 5–9. Point analyses within the mapped areas are shown within the mapped areas. See Data Set S2

**Table 4**  
The Summary of Bulk and Secondary Ion Mass Spectrometry (SIMS)  $\delta^{18}\text{O}$  and  $^{16}\text{OH}/^{16}\text{O}$  Measurements of MGL Opal-CT

| Sample      | $\delta^{18}\text{O}$ by laser fluorination (mean $\pm$ 2SD; in ‰) | VSMOW | $\delta\text{D}$ by TC/EA, ‰ | $\text{H}_2\text{O}$ by TC/EA (wt.%) | No. points by SIMS  | SIMS $\delta^{18}\text{O}$ mean $\pm$ 2D (‰, raw)       | SIMS $\delta^{18}\text{O}$ median, (‰, raw)           | SIMS $\delta^{18}\text{O}$ range (‰, raw) | SIMS mean (‰) | SIMS median (‰) | SIMS range (‰)   |
|-------------|--|-------|------------------------------|--------------------------------------|---|---|---|---|---------------|-----------------|--|
| MGL opal-CT | $27.99 \pm 0.93$   | -80‰  | 5.2                          | 89                                   | $26.5 \pm 2.0$  | 26.1  | 4.3   | 2.7                                       | 2.7           | 2.7             | $1,000 \times ^{16}\text{OH}/^{16}\text{O}$ range (‰)  |
|             |  |       |                              |                                      | $\delta^{18}\text{O}$ mean $\pm$ 2D (‰, normalized to UNILQ1) | $\delta^{18}\text{O}$ median, (‰, normalized to UNILQ1) | $\delta^{18}\text{O}$ range (‰, normalized to UNILQ1) |   |               |                 | $1,000 \times ^{16}\text{OH}/^{16}\text{O}$ median (‰) |
|             |  |       |                              |                                      | $32.1 \pm 1.1$  | 32.0  | 2.6   |   |               |                 | $1,000 \times ^{16}\text{OH}/^{16}\text{O}$ range (‰)  |

Note. The raw  $\delta^{18}\text{O}$  values are calculated from the measured  $^{18}\text{O}/^{16}\text{O}$  values. We also report values normalized to the  $\delta^{18}\text{O}$  of UNILQ1; note that these are not on VSMOW scale due to different instrumental mass fractionation displayed by MGL opal-CT.

for locations and representative electron microprobe point analyses along with the mapped areas combined with the microscope images of the SIMS points. Since the samples are extremely fine grained (<1  $\mu\text{m}$  grain size), it is not always possible to determine exact mineralogical forms of silica. The electron microprobe analyses of cherts yield  $\text{SiO}_2$  concentrations of 88–99 wt.%  $\text{SiO}_2$ . Since other measured impurities ( $\text{Al}_2\text{O}_3$ ,  $\text{K}_2\text{O}$ ,  $\text{CaO}$ , and  $\text{FeO}$ ) constitute <1 wt.% in the measured areas, we consider that samples with <99 wt.%  $\text{SiO}_2$  contain the complementary amount of  $\text{H}_2\text{O}$  that cannot be determined by electron microprobe directly. Thus, the electron microprobe measurements can identify hydrous opals, quartz and their mixtures. However, this is complicated by presence of 0–2 wt.% in chalcedony (Graetsch et al., 1985), which is a common constituent of cherts. Measurements of pure quartz grains included in the same sample holders yield 99.9 to 100.1 wt.%  $\text{SiO}_2$ . The MGL opal-CT returned 95.5 wt.%  $\text{SiO}_2$ , roughly consistent with the  $\text{H}_2\text{O}$  content of ~5 wt.% (see Data Set S2).

## 5. Discussion

### 5.1. The mm-Scale Homogeneity of $\delta^{18}\text{O}$ Values

The chert  $\delta^{18}\text{O}$  bulk values have a range between 32‰ and 38‰ in seafloor-drilled samples that have ages between 135 and 40 Ma, whereas the subaerial late Campanian (~84 to 72 Ma) Mishash formation chert has  $\delta^{18}\text{O}$  of 30‰. These values are consistent with previous measurement by conventional fluorination of the same samples (Kolodny & Epstein, 1976). The majority of microcrystalline cherts (excluding the porcellanite rinds; see Figure 1) measured as multiple 1–2 mg fragments by bulk laser fluorination have limited variability within individual sample, mostly within 1‰. Given that the analytical reproducibility of about 0.2‰ for the bulk laser fluorination, these variations can be ascribed to small differences in  $\delta^{18}\text{O}$  of the cherts (<1‰) at the scale of several mm. These variations could also reflect different amount of impurities present in cherts as can be noted by the variation in color (Figure 1). The fragment of porcellanite from the rind of the chert sample 195-20-4cc has a  $\delta^{18}\text{O}$  1.3‰ higher than the cherty part of the same sample (Figure 1). A similar result for this exact sample was found by Kolodny and Epstein (1976). Similarly, a porcellanite rind of the sample 167-17-33-127-129 is ~1‰ higher in  $\delta^{18}\text{O}$  than the cherty part. These differences were originally interpreted as the difference in the formation temperatures of opal-CT and microquartz during diagenesis (Kolodny & Epstein, 1976). This is now also documented in the downhole  $\delta^{18}\text{O}$  measurements of silica varieties separated from sediments that undergo diagenesis (Yanchilina et al., 2020). Having these samples extensively measured by bulk laser fluorination provides a well-calibrated target to explore the variability at the micrometer scale by SIMS.

### 5.2. The $\mu\text{m}$ -Scale Heterogeneity of $\delta^{18}\text{O}$ Values

The detailed microscale SIMS measurements show that the same samples display significant micrometer-scale  $\delta^{18}\text{O}$  heterogeneities exceeding the range of 1‰ measured by the bulk laser fluorination. Particularly, the three samples (195-20-4cc, 167-73-2-90-92 ad 466-9-1-65-65) exhibit  $\delta^{18}\text{O}$  variability ranging up to 6‰ (Figure 4). This range is best interpreted as variations in the petrographic variety as identified by their water content with the simultaneous  $^{16}\text{OH}/^{16}\text{O}$  measurements (see Figure 5). In sample 195-20-4cc the high- $^{16}\text{OH}/^{16}\text{O}$  domains correspond to low  $\delta^{18}\text{O}$  values, extending by about ~4‰ below the mean value determined by laser fluorination. The high- $^{16}\text{OH}/^{16}\text{O}$  domains only occur in the fragments of chert that include zones of porcellanite (see Figure 5) and are likely subjected to the effects of hydration water (see Figure 3). The mapped Si- and Al-concentrations are distinctly higher in these hydrous domains compared to the low- $^{16}\text{OH}/^{16}\text{O}$  domains (Figure 5). Such areas have  $\text{SiO}_2$  <96 wt.% (as low as 88 wt.%) corresponding to several wt.%  $\text{H}_2\text{O}$  and, thus, are interpreted as areas of opaline silica. The Al-concentrations range between 0 and 1 wt.% and display faint patterns of radiolarian molds and clay particles as seen in the mapped Al-concentrations (Figure 5). Given that common clays (e.g., illite) contain close to 20 wt.%  $\text{Al}_2\text{O}_3$ , the low  $\text{SiO}_2$  (and hence high  $\text{H}_2\text{O}$ ) is likely due to presence of hydrous opal, while clays are a common impurity (up to 5 wt.% based

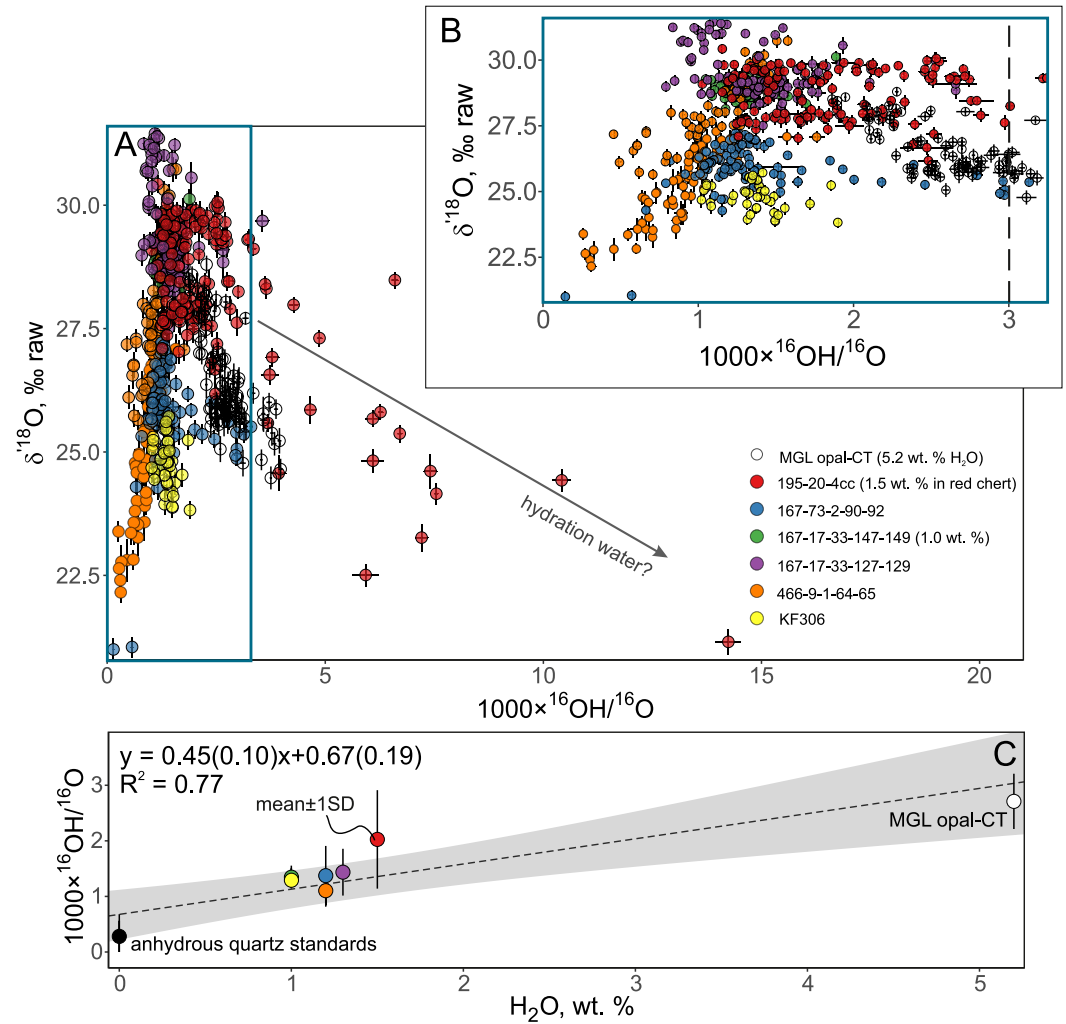


**Figure 3.** (a) Raw  $\delta^{18}\text{O}$  values plotted against  $1000 \times {}^{16}\text{OH}/{}^{16}\text{O}$  measured in the MGL opal-CT and chert samples. A prominent negative correlation between the  $1000 \times {}^{16}\text{OH}/{}^{16}\text{O}$  and  $\delta^{18}\text{O}$  is observed in MGL opal-CT and hydrous domains of sample 195-20-4cc. This correlation is however absent in chert samples with  $1000 \times {}^{16}\text{OH}/{}^{16}\text{O}$  below  $\sim 3$ . (b) Inset showing the measurements with  ${}^{16}\text{OH}/{}^{16}\text{O}$  below 3‰. This value is used as a cut-off for reducing the chert raw data to VSMOW scale using the anhydrous quartz standards. The  ${}^{16}\text{OH}/{}^{16}\text{O}$  and  $\delta^{18}\text{O}$  values in sample 466-9-1-64-65 are positively correlated, which is interpreted as a two-component mixing between different varieties of silica (see Section 5). (c) The  $\text{H}_2\text{O}$  wt.% determined by bulk TC/EA plotted against the  ${}^{16}\text{OH}/{}^{16}\text{O}$  measurements by secondary ion mass spectrometry. The equation and  $R^2$  value of the linear regression are shown. The uncertainties on the regression terms are given in the parenthesis.

on formula of illite). The SIMS-determined  ${}^{16}\text{OH}/{}^{16}\text{O}$  ratios reach up to 14‰ in these areas, while the  $\delta^{18}\text{O}$  values range between 29‰ and 35‰. However, as discussed earlier (see Section 4) the areas with low  $\delta^{18}\text{O}$  are likely subjected to the effects of hydration water as indicated by the  ${}^{16}\text{OH}/{}^{16}\text{O}$  ratios above 3‰. Meanwhile, the microquartz and chalcedony aggregates are dispersed within porcellanite and compose the majority of the red cherty part of the sample (see Figure 1). They frequently compose radiolarian molds. Such aggregates have  $\delta^{18}\text{O}$  ranging between 33‰ and 36‰ and low  ${}^{16}\text{OH}/{}^{16}\text{O}$  values below 3‰ (see Figure 5). In addition, the microprobe measurements yield  $\text{SiO}_2$  concentrations above 96 wt.% in these areas, while the bulk TC/EA measurement of the red cherty part of the sample yields 1.5 wt.%  $\text{H}_2\text{O}$ . It is likely that the microquartz contain some Si-OH groups and/or minor opal and clay particles giving it moderate  ${}^{16}\text{OH}/{}^{16}\text{O}$  values and less variable  $\delta^{18}\text{O}$ . Unlike the porcellanite fragments, these quartz-dominated parts of chert have mean SIMS  $\delta^{18}\text{O}$  values that are in agreement with the  $\delta^{18}\text{O}$  values measured by bulk laser fluorination.

The sample 167-73-2-90-92 has domains with  $\delta^{18}\text{O}$  values about 4‰–5‰ lower than the mean value (Figure 6). These areas correspond to the rare occurrences of silica fillings inside of the radiolarian tests that have  $\delta^{18}\text{O}$  of

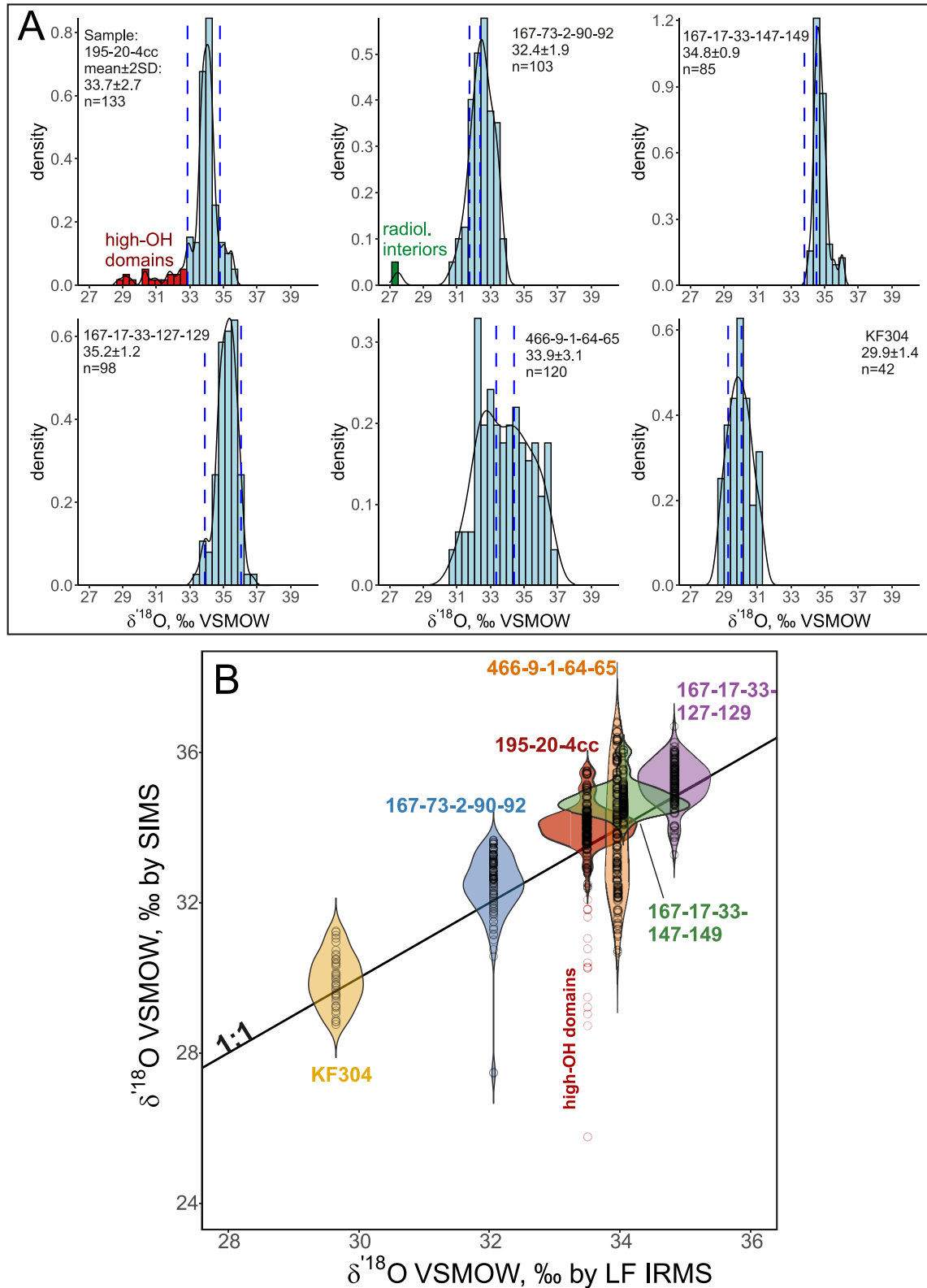


**Figure 4.** (a) Secondary ion mass spectrometry (SIMS)-determined values  $\delta^{18}\text{O}$  plotted as histograms for each sample. The histograms are plotted with the kernel density function (black curves), while vertical blue dashed lines indicate the range of  $\delta^{18}\text{O}$  values measured by bulk laser fluorination. The mean  $\pm$  2SD are shown for each sample. (b) The SIMS  $\delta^{18}\text{O}$  values are plotted as violin plots against the average bulk values determined by laser fluorination isotope ratio mass spectrometry (LF IRMS).

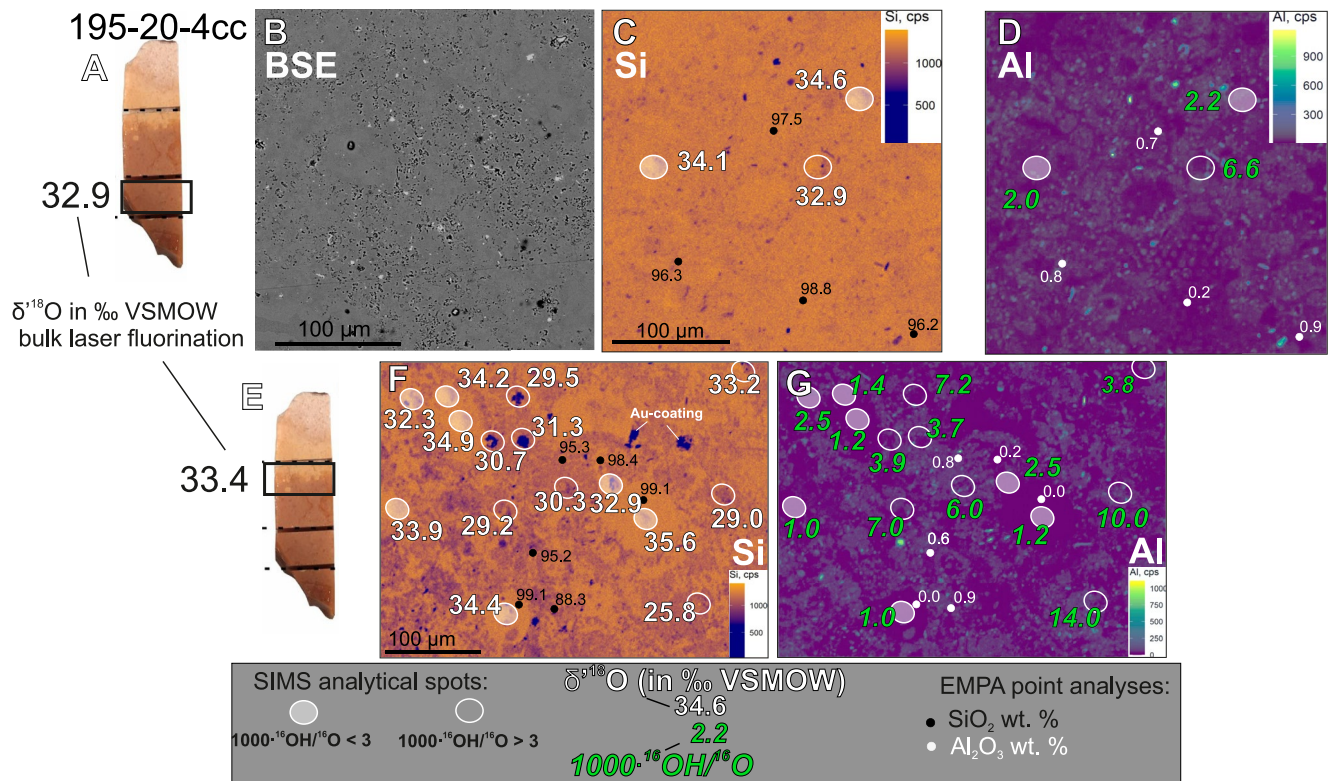


**Figure 5.** The  $\delta^{18}\text{O}$  values measured by secondary ion mass spectrometry (SIMS) in different parts of sample 195-20-4cc. The first row of images (a through d) shows the red cherty part analyzed by bulk laser fluoration (outlined in panel a). Panel (b) shows a back-scattered electron (BSE) image of a representative area of the chert. Panels (c and d) show color-coded electron microprobe Si- and Al-concentration maps with SIMS measurements shown with white ellipses. Labeled points show  $\delta^{18}\text{O}$  (‰ VSMOW) values and  $1000 \cdot ^{16}\text{OH}/^{16}\text{O}$  values as represented in the legend. The ellipses filled with transparent white color correspond to the  $1000 \cdot ^{16}\text{OH}/^{16}\text{O}$  below 3 (see legend). The dots show point analyses by electron microprobe with wt.% of  $\text{SiO}_2$  and  $\text{Al}_2\text{O}_3$ . The second row (e through g) of panels features the fragment of sample adjacent to the porcellanite rind. The sample contains many hydrous high- $^{16}\text{OH}/^{16}\text{O}$  domains correlating with low  $\delta^{18}\text{O}$  values (see Figures 3 and 4).

about 27.5‰. One such area is depicted in Figure 6. However, outside of these rare areas, this sample has less variability in  $\delta^{18}\text{O}$  with values between 30‰ and 34‰, even though the petrographic varieties of silica include microquartz, chalcedony and opal (Figure 6). We suggest the rare occurrence of low- $\delta^{18}\text{O}$  fillings in the radiolarian tests depict precipitation of late-stage silica at high temperature and/or from  $^{18}\text{O}$ -depleted marine pore water fluids, which could be negative in  $\delta^{18}\text{O}$  (e.g., Lawrence et al., 1975). The radiolarian tests are clearly identified in a polarized microscope as they are composed of isotropic opal and are filled with radiating chalcedony, showing systematically lower Si concentrations (Figure 6). The microcrystalline matrix of this sample is extremely fine grained. Two distinct silica forms are visible in the grayscale brightness of the BSE images. The matrix is thus likely composed of microquartz and opal (or chalcedony) with  $\text{SiO}_2$  content between 90 and 96 wt.%. Nonetheless, the  $\delta^{18}\text{O}$  values measured by SIMS are indistinguishable between the matrix and the skeletal silica. The  $^{16}\text{OH}/^{16}\text{O}$  are on average higher in the opal and chalcedony of the radiolarian tests, up to 2.0‰, while the microcrystalline matrix has  $^{16}\text{OH}/^{16}\text{O}$  ratios of around 1‰. We do not observe any correlation between the  $^{16}\text{OH}/^{16}\text{O}$  and  $\delta^{18}\text{O}$  ratios, assuming that there is no effect of hydration water in the opaline silica and microquartz matrix in this particular sample.

The sample 466-9-1-64-65 has 2SD of 3.1‰, with  $\delta^{18}\text{O}$  values ranging between 30‰ and 37‰. Petrographically, the sample is microcrystalline, with numerous ghostly recrystallized fossils that are recognizable by the slight petrographic difference in the crystallinity of silica (Figure 7). We find no relation between the  $\delta^{18}\text{O}$  values and petrographic appearance of the analyzed area. We however note that this sample has a positive correlation between  $\delta^{18}\text{O}$  and  $^{16}\text{OH}/^{16}\text{O}$  (Figure 3). Other samples have a similar range of  $^{16}\text{OH}/^{16}\text{O}$  ratios, between 0‰ and 1.5‰, but without a correlation with  $\delta^{18}\text{O}$ . Further, the bulk TC/EA measurements of the sample yield 1.2 wt.%  $\text{H}_2\text{O}$ , which is within the range of the rest of the samples (between 1.0 and 1.5 wt.%). We thus interpret that this sample is composed of low- and high- $^{16}\text{OH}/^{16}\text{O}$  domains of silica that have respectively lower and higher  $\delta^{18}\text{O}$

167-73-2-90-92

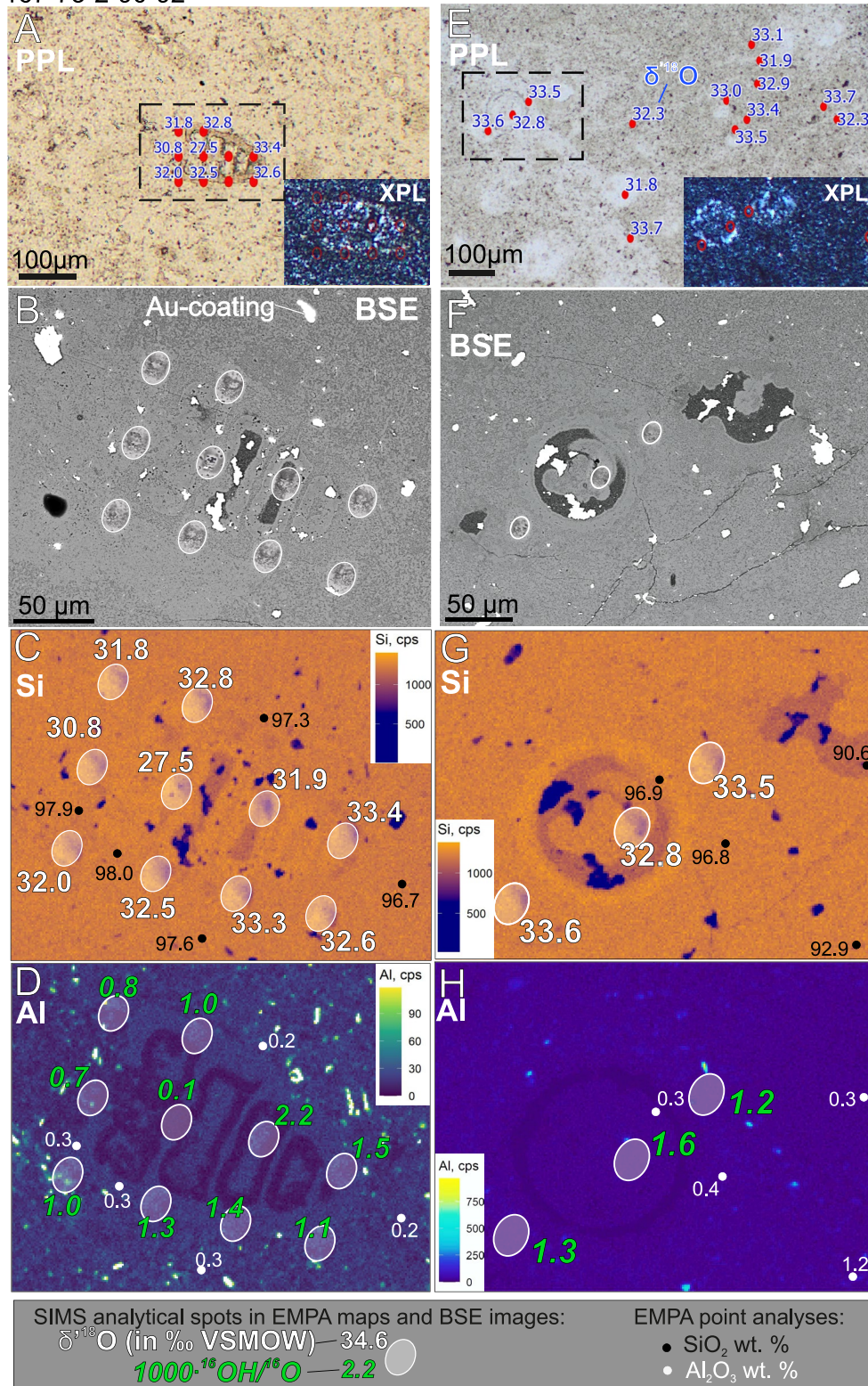
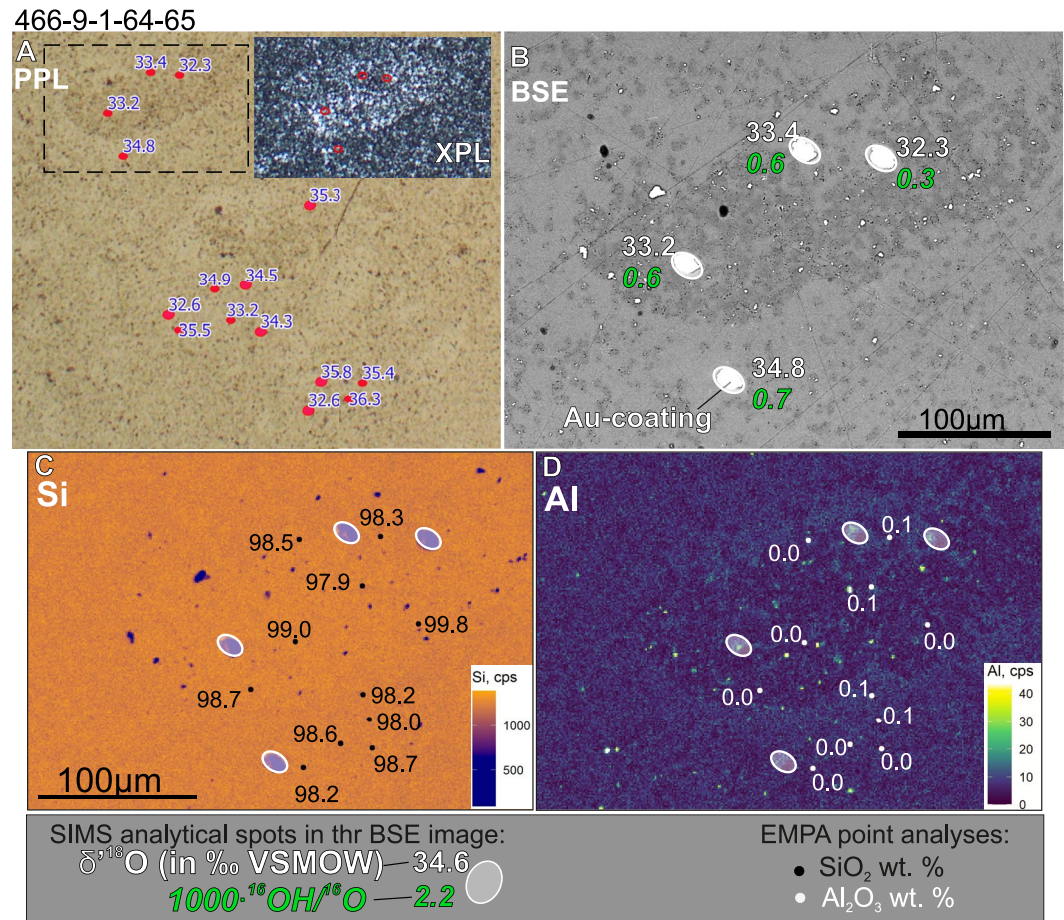


Figure 6.



**Figure 7.** A representative area in sample 466-9-1-64-65 measured for  $\delta^{18}\text{O}$ - $^{16}\text{OH}/^{16}\text{O}$  by secondary ion mass spectrometry (SIMS). The area is shown in panels (a–d): (a) plane (PPL) and cross (XPL) polarized light with the area of interest outlined, (b) back-scattered electron (BSE) image of the analyzed area. Panels (c and d) show Si- and Al-concentration electron microprobe maps, respectively. Note that the sample is represented by a fine mixture of silica species visible as the patchy texture in the BSE image. The bright white spots in the BSE image are the SIMS spots showing remnants of gold coating.

values. It is difficult to document the distinction between the endmembers, since the back-scattered electron images shows microscopic size of two silica phases (Figure 7), comparable in size to that of the SIMS points. However, it is likely that the microscopic hydrous phase is opal-CT and/or chalcedony finely mixed with micro-quartz. Moreover, the mean SIMS  $\delta^{18}\text{O}$  value agrees well with the values measured by bulk laser fluorination, highlighting the microscopic scale of isotope variability. The aggregate has a low  $\text{H}_2\text{O}$  content since it has some of the lowest  $^{16}\text{OH}/^{16}\text{O}$  in our data set, and the microprobe point analyses yield  $\text{SiO}_2 > 97$  wt.% (see Data Set S2). Consequently, we identify these  $\delta^{18}\text{O}$  SIMS variations between 30‰ and 37‰ as a range of values of silica in the sample.

### 5.3. Samples With $\delta^{18}\text{O}$ Heterogeneities Below 2‰

The samples from cores 167-17-33-147-149, 167-17-33-127-129 as well as the subaerially sampled Mishash formation chert (KF304) all have smaller  $\delta^{18}\text{O}$  variability. The SIMS  $\delta^{18}\text{O}$  values in these samples vary within

**Figure 6.** Two representative areas of sample 167-73-2-90-92 featuring radiolarian tests and matrix measured for  $\delta^{18}\text{O}$ - $^{16}\text{OH}/^{16}\text{O}$  by secondary ion mass spectrometry (SIMS). The first area is depicted in panels (a) through (d) in: (a) plane (PPL) and cross (XPL) polarized light with area of interest outlined with a dashed rectangle, (b) back-scattered electron (BSE) image, (c and d) electron microprobe Si- and Al-concentration maps. These images show a rare occurrence of silica with  $\delta^{18}\text{O} = 27.5$ ‰ found within the radiolaria test. Due to high Si-content, low  $^{16}\text{OH}/^{16}\text{O}$  such area are likely aggregates of microquartz. The second area is shown in panels E through H in same order. The interior of radiolarian tests in these images (e through h) contain highly hydrous form of opal with  $\text{SiO}_2$  content of 91 wt.%. It is also visible that the matrix of the chert is heterogeneous and is made from two forms of silica that have different gray scale brightness in the BSE images.

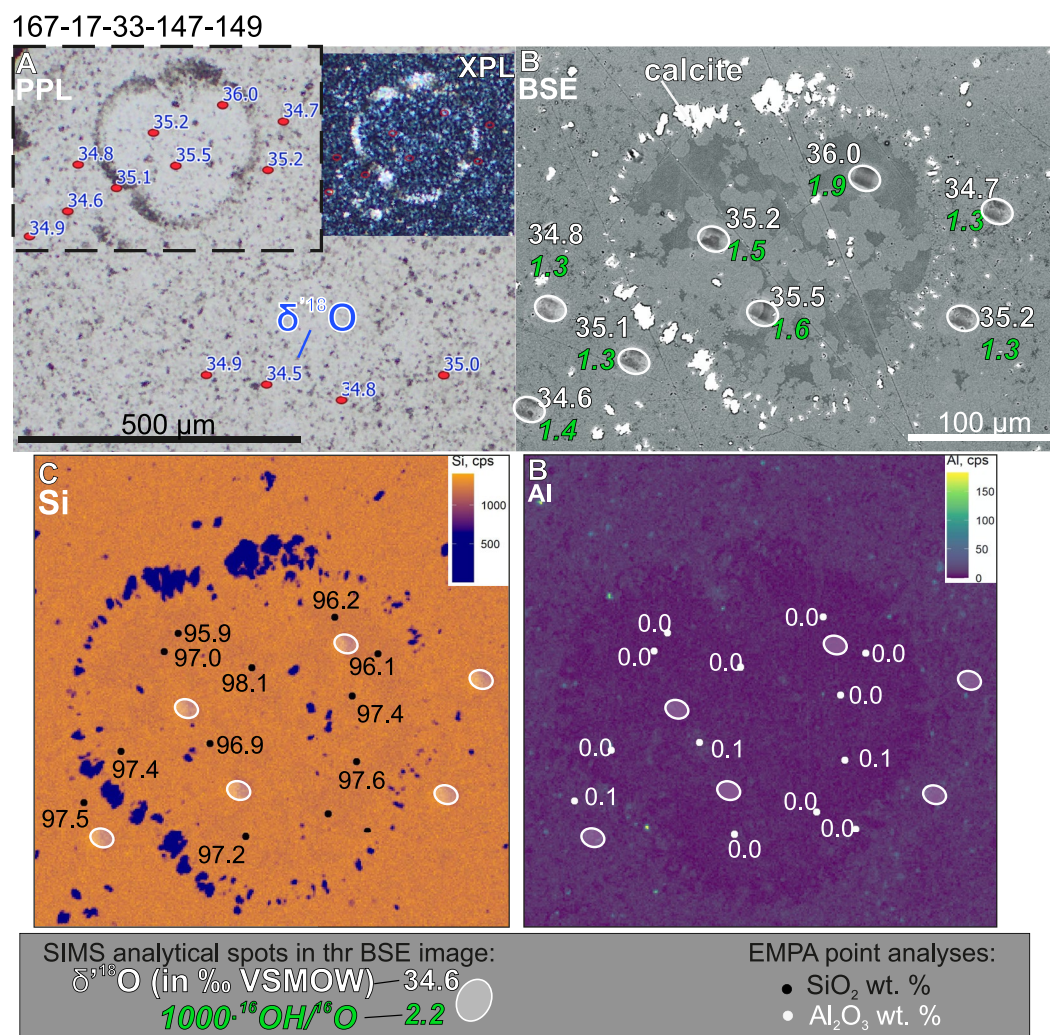


**Figure 8.** A representative area in sample 167-17-33-147-149 measured for  $\delta^{18}\text{O}$ - $^{16}\text{OH}/^{16}\text{O}$  by secondary ion mass spectrometry (SIMS) depicted in plane and cross polarized light, back-scattered electron images and microprobe elemental maps. The area is shown in panels (a–d): (a) plane (PPL) and cross (XPL) polarized light with the area of interest outlined, (b) back-scattered electron (BSE) image of the analyzed area. Panels (c and d) show Si- and Al-concentration electron microprobe maps, respectively. Note that the sample is represented by a fine mixture of silica species visible as the patchy texture in the BSE image. The bright white spots in the BSE image are the SIMS spots showing remnants of gold coating. The area contains a recrystallized carbonate foraminifera test (labeled calcite in panel (b)), which is filled with a variety of hydrous opal with  $\text{SiO}_2$  content of  $\sim 96$  wt.%. The surrounding aggregate likely consists of microquartz and chalcedony.

the total range of about 2‰ and with the mean values closely matching the bulk laser fluorination measurements (Figure 4). The seafloor-drilled cherts (167-17-33-147-149, 167-17-33-127-129) have an average value  $\delta^{18}\text{O}$  of 35‰. They contain considerable amount of carbonate in form of foraminifera test that are filled with fibrous and opaline silica with  $\delta^{18}\text{O}$  values similar (within 1‰) to those of the microcrystalline matrix, despite the clear petrographic difference (Figure 8). Demonstrably, chert 167-17-3-147-149 displays carbonate tests filled with a characteristic spherulitic aggregate of opal-CT (Figure 8) with  $\delta^{18}\text{O}$  values around 35‰–36‰, while the matrix around the test has comparable values around 35‰. The limited variability of  $\delta^{18}\text{O}$  values in these samples is perplexing, since we notice that other cherts (e.g., 195-20-4cc, 167-13-2-90-92) also contain various petrographic forms of silica (e.g., high- $^{16}\text{OH}/^{16}\text{O}$  opal and radiolarian test fillings), however, their  $\delta^{18}\text{O}$  values are a lot more variable at microscale.

The chert from Mishash formation contains microquartz (Figure 9) that petrographically appears to be free of opaline silica. No fossils are observed in the sample, and the chemical composition and petrographic texture of microquartz are homogenous. The sample exhibits  $\text{SiO}_2$  content between 97 and 98 wt.% and  $^{16}\text{OH}/^{16}\text{O}$  ratios

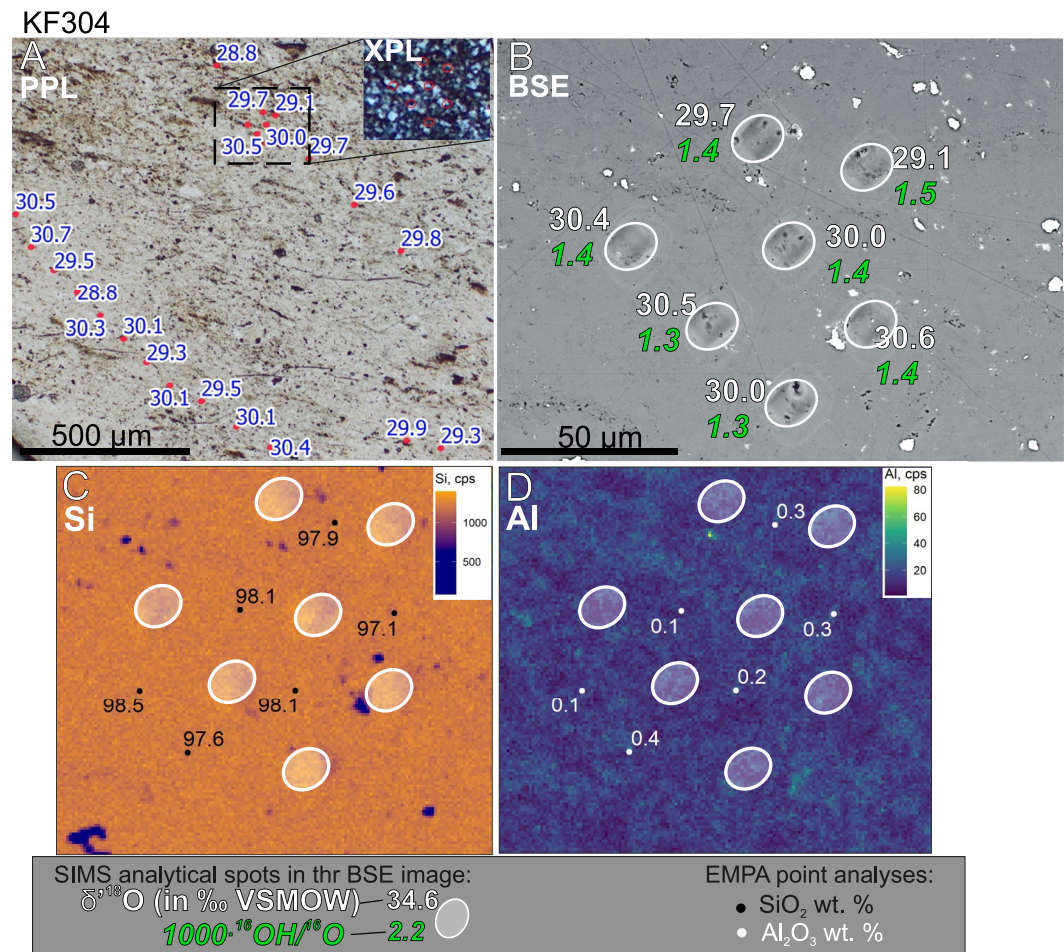


**Figure 9.** Representative images of  $\delta^{18}\text{O}$ – $^{16}\text{OH}/^{16}\text{O}$  secondary ion mass spectrometry (SIMS) measurements in the subaerially sampled Mishash formation chert (KF304). The area is shown in panels (a–d): (a) plane (PPL) and cross (XPL) polarized light with the area of interest outlined, (b) back-scattered electron (BSE) image of the analyzed area. Panels (c and d) show Si- and Al-concentration electron microprobe maps, respectively. The bright white spots in the BSE image are remnants of gold coating and rare impurities of iron oxides (see Data Set S2).

around 1.0‰–1.5‰, similar to the microquartz from the seafloor-drilled cherts. The  $\delta^{18}\text{O}$  of this sample is tightly constrained to  $30\text{‰} \pm 1\text{‰}$  and does not correlate with the  $^{16}\text{OH}/^{16}\text{O}$  ratio. The variability within these samples is narrow and bell-shaped in  $\delta^{18}\text{O}$ , and comparable to that of the bulk laser fluorination measurements (see Figure 4). Previous research (Kolodny et al., 1980) reports a large range of bulk chert  $\delta^{18}\text{O}$  values from the Mishash formation between 21‰ and 35‰. The high  $\delta^{18}\text{O}$  values within the range are found in homogeneous cherts, while more diverse and low  $\delta^{18}\text{O}$  values are measured in the matrix of brecciated cherts (Kolodny et al., 1980). The interpretation of the basin and the oxygen isotope data suggests that cherts initially precipitated from evaporated ocean water and then were later silicified during a shallow (<1,000 m) burial diagenesis in presence of fresh meteoric-derived fluids. Our sample corresponds to the homogeneous cherts from the Mishash formation. The relatively homogeneous O-isotope composition of the chert at the microscale indicates that interaction with the second-stage later meteoric-derived fluids have not affected the cherts outside of the areas of brecciation, where recrystallization is evident.

In summary, some seafloor-drilled cherts are heterogeneous with up to 6‰ variation in  $\delta^{18}\text{O}$  value, while others exhibit variability below 1‰. The  $\delta^{18}\text{O}$  variability and its relationship to the petrographic features are sample-dependent. This is in contrast with the relatively narrow range of about 1‰ measured by bulk extraction techniques for several fragments of the same samples. The difference in the  $\delta^{18}\text{O}$  variability is likely due to the difference in diagenetic history of the samples. In addition, some difference in diagenetic scheme is expected due to the different contents of carbonates and clays in the lithological context (see Table 1). Presence of other

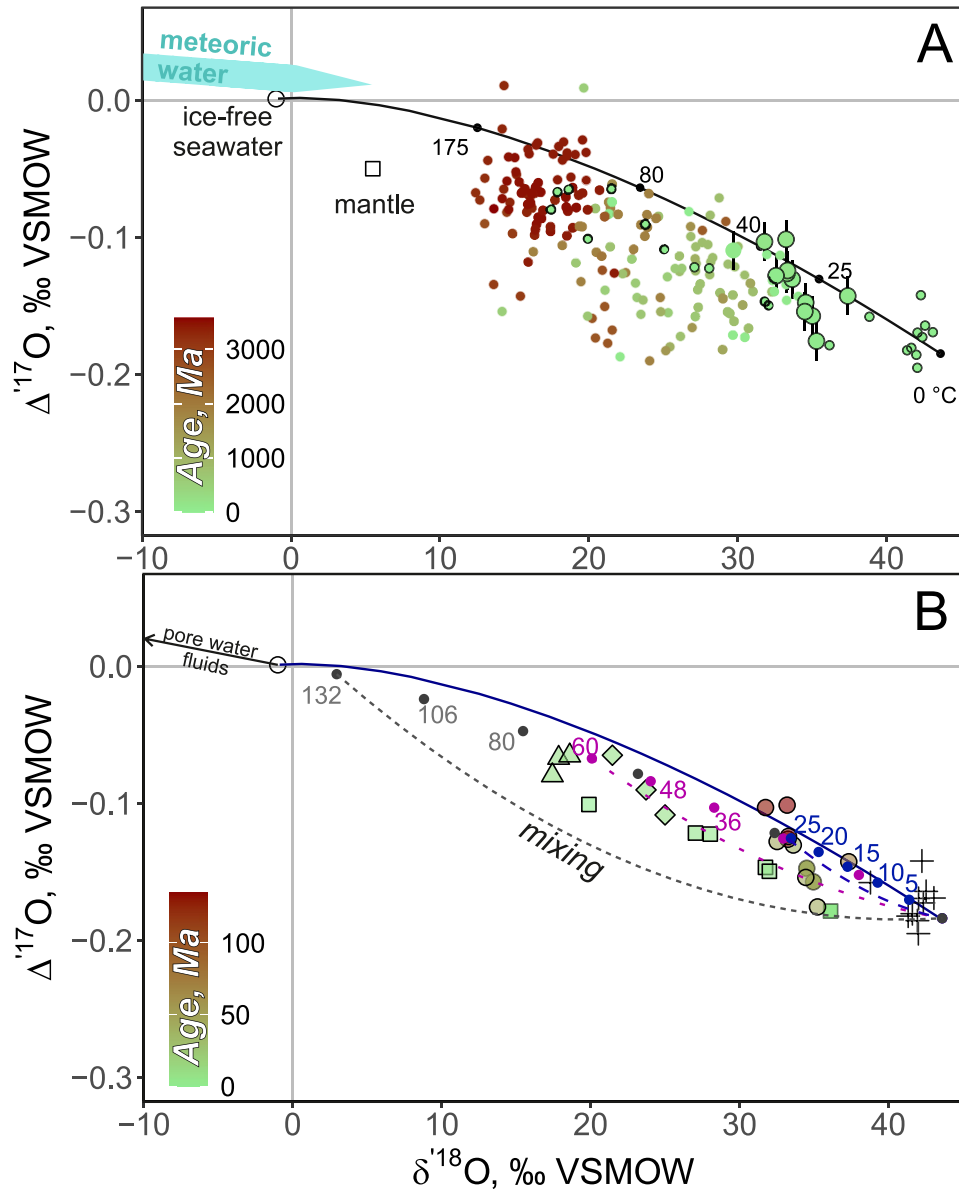
substances like carbonates or clays within the sediment affects the diagenetic solubility of opal-A, opal-CT and quartz during chert diagenesis (Williams et al., 1985). The abundance of carbonates in the cherts with limited  $\delta^{18}\text{O}$  variability ( $<1.5\text{‰}$ ) hints at the role of carbonates in the rate of silica transformations (e.g., Lancelot, 1973). Samples with limited variability (167-17-33-147-149, 167-17-33-127-129) contain abundant carbonate in form of recrystallized foraminifera tests that are evident in thin sections and the Ca-concentration maps. Other cherts contain microscopic clays, which are reflected in the elevated mapped Al- and K-concentrations (see Data Set S2 for K-concentration maps) in cherts 195-20-4cc and 167-73-2-90-92. In addition, we document rare detectible variations in Fe-concentrations in some samples (195-20-4cc and KF304; see Data Set S2), likely corresponding to iron-oxide films, which in turn give the samples their reddish color (Figure 1). The cherts with impurities of clay tend to exhibit heterogeneities in  $\delta^{18}\text{O}$  and presence of diverse forms of silica (opaline radiolarian tests and microquartz). These observations concur to the previous studies that found that clay impurities slow down the rates of mineralogical transformations from biogenic silica (opal-A) to opal-CT, potentially promoting formation of silica species with different  $\delta^{18}\text{O}$  at different depths and temperatures (e.g., Hinman, 1998; Williams et al., 1985; Yanchilina et al., 2021). A prolonged formation of silica in seafloor conditions would result in heterogeneous  $\delta^{18}\text{O}$  values measured in-situ by SIMS. However, to confirm the origin of the heterogeneities due to the lithological control, more  $\delta^{18}\text{O}$  measurements by SIMS are needed, ideally targeting drilled down-hole profiles in parts of oceans dominated by different sediments. Thus, using electron microprobe mapping of common constituents such as Si and Al combined with quantitative point analyses, provides an additional tool to understand the mineralogical control on diagenesis and consequent evolution of  $\delta^{18}\text{O}$  values.

Our measurements present the first  $\delta^{18}\text{O}$  results obtained by SIMS for the modern-day seafloor-drilled cherts, showing that the microscale heterogeneities between 2‰ and 6‰ originate already in the seafloor environment. This is relevant because microscale  $\delta^{18}\text{O}$  heterogeneities are also found in Precambrian cherts (e.g., Cammack et al., 2018; Marin-Carbonne et al., 2014) that precipitated abiotically, presumably from silica gels (Stefurak et al., 2015). These heterogeneities are frequently interpreted as products of post-depositional recrystallization and metamorphism well after their seafloor diagenesis, obscuring the secular O-isotope evolution of the hydrosphere and seawater temperature.

#### 5.4. The $\delta^{18}\text{O}$ — $\Delta^{17}\text{O}$ Systematics of Deep-Sea Cherts

Similar to previous measurements of cherts (Hayles et al., 2019; Liljestr and et al., 2020; Lowe et al., 2020; Sengupta et al., 2020; Zakharov, Marin-Carbonne, et al., 2021), our data partially overlap with the equilibrium quartz fractionation curve assuming ice-free seawater composition of equilibrium fluid, that is,  $\delta^{18}\text{O} = -1\text{‰}$  (see Figure 2). However, as for most of the chert data across geological time, our cherts plot under the curve, that is, with  $\Delta^{17}\text{O}$  and  $\delta^{18}\text{O}$  lower than predicted by the equilibrium fractionation curve (Figure 10). Our data spanning between 135 and 40 Ma fill the gap between the older cherts, extending back to Archean, and the more recent/modern diatoms and siliceous sediments (see compilation of data in Figure 10a). The data is also distinct from the older Phanerozoic and Precambrian cherts in that it plots close to the low-temperature range of the equilibrium fractionation, near the apparent equilibrium temperatures around 25°C–40°C. Some of our 135–130 Ma cherts plot on the equilibrium line, while younger cherts have lower  $\Delta^{17}\text{O}$  values and consequently plot below the line (Figure 10). Compared to the Precambrian and older Phanerozoic cherts that plot under the 100°C–175°C region of the equilibrium curve, the  $\Delta^{17}\text{O}$  of studied here cherts are similarly shifted downwards. The subaerially exposed Cretaceous chert KF304 plots similarly close and under the silica-seawater equilibrium curve despite being potentially exposed to meteoric water fluids.

This departure from the equilibrium fractionation toward low  $\Delta^{17}\text{O}$  can be explained by recrystallization of silica in sedimentary conditions. The temperature during diagenesis is higher compared to the ambient seawater and is controlled by the depth of burial and heat flux through the oceanic plate. Increasing the temperature during diagenesis and subsequent recrystallization in presence of buried seawater would decrease  $\delta^{18}\text{O}$  and increase  $\Delta^{17}\text{O}$  in accord with the seawater-silica fractionation line (Sharp et al., 2016). Further, due to the reactivity of buried seawater within the oceanic crust and precipitation of minerals with high  $\delta^{18}\text{O}$  (Savin & Epstein, 1970), marine pore water fluids often exhibit negative  $\delta^{18}\text{O}$  gradients, mostly between  $-15$  and  $-2\text{‰/km}$ , indicative of the low-temperature nature of reactions below or within sediment (Gieskes, 1981; Gieskes & Lawrence, 1981; Lawrence et al., 1975; Lawrence & Gieskes, 1981). Diagenetic recrystallization in the presence of reacted pore water fluids would result even in more notable departure of cherts from the original seawater-silica equilibrium



| Explanation to B  |  |
|---|--|
| Silica calculated for   | 132 °C/km; -13.5 ‰/km                  |
| T- and pore water δ <sup>18</sup> O gradients:  | 60 °C/km; -7 ‰/km<br>25 °C/km; -2 ‰/km |
| Siliceous sediments from present-day seafloor:  |  |
| Marine diatoms from 0.4-0.1 Ma sediments from the Southern Ocean (Sharp et al., 2016) | +                                      |
| 10-0 Ma diatom oozes and cherts from the Sea of Japan (Ibarra et al., 2022)           | △ microquartz<br>□ opalA ◇ opalCT      |
| 40-135 Ma deep-sea cherts from the Pacific and Atlantic Oceans (this study)           | ○                                      |

Figure 10.

line. Such pore water fluids have negative  $\delta^{18}\text{O}$  values and likely slightly positive or near-zero  $\Delta^{17}\text{O}$  values (McGunnigle et al., 2022; Zakharov, Tanaka, et al., 2021) due to precipitation of low- $\Delta^{17}\text{O}$  clays (Sengupta & Pack, 2018). While oceanic geothermal gradients and pore water fluids are variable, depending on the age of the plate (i.e., distance from the axis) and nature of sediments, we show the possible compositions of recrystallized cherts that originally precipitated from seawater with  $\delta^{18}\text{O}$  of  $-1\text{‰}$  (Figure 10b). Mixing between the initial silica that precipitated at  $0\text{--}4^\circ\text{C}$  (i.e., diatoms) and recrystallized silica at depth covers a compositional field in the  $\delta^{18}\text{O}\text{--}\Delta^{17}\text{O}$  coordinates compatible with the existing chert data for seafloor, including the recently published measurements from the Sea of Japan (Ibarra et al., 2022). This mixing is calculated from a simple mass balance approach, assuming that the measured chert is a mixture of compositions:  $\delta^{18}\text{O}$  and  $\Delta^{17}\text{O}$  from the original precipitation (primary silica e.g., diatoms) and a new  $\delta^{18}\text{O}$  and  $\Delta^{17}\text{O}$  composition that formed under subseafloor conditions. The final composition can be calculated using the fraction ( $f$ ) of primary seawater-derived isotope composition:

$$\delta^{17/18}\text{O}_{\text{chert}} = f \cdot \delta^{17/18}\text{O}_{\text{primary}} + (1 - f) \cdot \delta^{17/18}\text{O}_{\text{diagenetic}}, \quad (1)$$

Equation 1 can be rewritten in terms of equilibrium fractionation:

$$\delta^{17/18}\text{O}_{\text{chert}} = f \cdot (\delta^{17/18}\text{O}_{\text{seawater}} + 1000 \ln^{18/17} \alpha_{\text{H}_2\text{O-silica}}) + (1 - f) \cdot (\delta^{17/18}\text{O}_{\text{porewater}} + 1000 \ln^{18/17} \alpha_{\text{H}_2\text{O-silica}}), \quad (2)$$

where  $1000 \ln^{18/17} \alpha_{\text{H}_2\text{O-silica}}$  are the calibrated temperature-dependent fractionation factors for triple O-isotope equilibrium (Sharp et al., 2016). Using these expressions, we show the two possible generalized compositions of diagenetically recrystallized cherts for geothermal profiles of old and young oceanic plates assuming the geothermal gradients of 25 and  $60^\circ\text{C}/\text{km}$ . These are coupled, respectively, with the pore water gradients of  $-7$  to  $-2\text{‰}/\text{km}$  that are typical for sedimentary pore water in the global ocean (Lawrence et al., 1975). These calculated compositions are highlighted by the seafloor-drilled deep-sea cherts from this study and the silica varieties that were diagenetically recrystallized in young and hot oceanic crust (Ibarra et al., 2022).

While temperature and marine pore water fluids control the  $\delta^{18}\text{O}\text{--}\Delta^{17}\text{O}$  values of final diagenetic silica, the values of primary silica (e.g., diatoms or radiolaria) play an important role in the final chert value (Figure 10). Currently, a limited number of studies addresses the biogenically mediated silica-water triple O-isotope fractionation (see Liljestr nd et al., 2021). The observed  $\Delta^{17}\text{O}$  fractionation yields values very close to the empirical calibration at low temperatures (Sharp et al., 2016; Wostbrock et al., 2018). However, the effect of post-mortem exchange in diatom frustules, which could be significant (e.g.,  $>7\text{‰}$  for  $\delta^{18}\text{O}$  in Dodd et al., 2012), has not been resolved in the triple O-isotope coordinates. Yet, it has a potential to influence the isotope composition of diagenetically mature chert.

Further, we expand the possible field of diagenetic solutions to a wider range of diagenetic conditions (Figure 11). These compositions cover ca. 90% of the Phanerozoic data younger than 135 Ma, when the seawater  $\delta^{18}\text{O}\text{--}\Delta^{17}\text{O}$  were unlikely to have varied significantly from the realm of ice-free conditions, that is,  $\delta^{18}\text{O} = -1\text{‰}$  and near-zero  $\Delta^{17}\text{O}$ . Given the previous studies of silica diagenetic transition, the triple O-isotope composition of cherts is in accord with the last final diagenetic isotope compositions at temperatures ranging between  $\sim 30^\circ\text{C}$  and  $\sim 165^\circ\text{C}$  (Behl et al., 1994; Williams & Crerar, 1985; Williams et al., 1985; Yanchilina et al., 2020). Further, in the generalized diagram we show a range of marine pore water fluids that could have assisted recrystallization. The diagram shows cases, where marine pore water fluids reach  $\delta^{18}\text{O}$  values as low as  $-10\text{‰}$  evolving toward slightly posi-

**Figure 10.** (a) Triple O-isotope compilation of chert and silica measurements across the geological time scale (Hayles et al., 2019; Ibarra et al., 2022; Levin et al., 2014; Liljestr nd et al., 2020; Lowe et al., 2020; Sengupta et al., 2020; Sharp et al., 2016; Zakharov, Marin-Carbonne, et al., 2021). The points are color-coded according to their age. Samples from the present seafloor setting are outlined with black circles and color-coded in bright green due to their young age. Cherts from this study are shown with larger symbols with vertical error bars (2SE). The solid black curve indicates silica-seawater equilibrium fractionation with temperatures labeled between  $0^\circ\text{C}$  and  $175^\circ\text{C}$  (fractionation from Wostbrock and Sharp (2021)). (b) The panel depicts possible recrystallization trajectories of siliceous sediments at different geothermal and pore water gradients. Diagenetic silica fully in equilibrium with pore water fluids between 0 and 1,000 m below seafloor are shown at 200-m intervals color-coded by different geothermal and pore water profiles. Equilibrium compositions are shown for a combination of profiles shown in gray ( $132^\circ\text{C km}^{-1}$ ,  $-13.5\text{‰ km}^{-1}$ ), pink ( $60^\circ\text{C km}^{-1}$ ,  $-7\text{‰ km}^{-1}$ ), and blue ( $25^\circ\text{C km}^{-1}$ ,  $-2\text{‰ km}^{-1}$ ). These gradients represent a range of diagenetic conditions present in areas of young oceanic crust (e.g., the Sea of Japan with steep  $132^\circ\text{C km}^{-1}$  geothermal and  $-13.5\text{‰ km}^{-1}$  pore water gradients) and older oceanic crust that has lower heat fluxes resulting in more gentle gradients (e.g.,  $25^\circ\text{C km}^{-1}$ ). While these combinations of temperature and pore water gradients are not unique, they are illustrative of possible recrystallization trajectories during diagenesis of cherts. The gray, pink, and blue dashed lines represent mixing between the original silica (e.g., post-mortem diatoms) and the diagenetic silica that is calculated from the respective geothermal and pore water profiles. The data points color-coded by age represent seafloor-drilled cherts from (Ibarra et al., 2022) and this study.

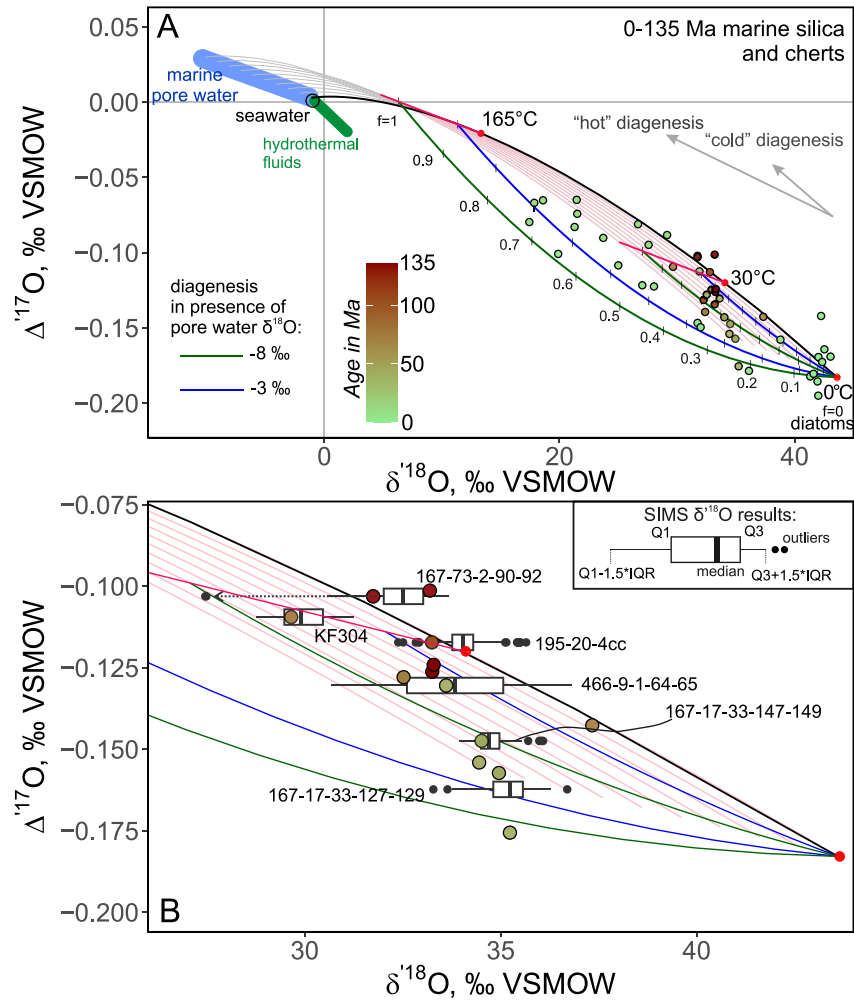


**Figure 11.** (a) Generalized model for marine diagenesis in recent cherts (0–135 Ma). Silica-seawater equilibrium is shown as the solid black curve, while the pink curves represent silica crystallized from marine pore waters with  $\delta^{18}\text{O}$  between  $-10\text{‰}$  and  $-1\text{‰}$ . Possible recrystallized end-members are shown here with straight red lines emerging from red circles labeled  $30^\circ\text{C}$  and  $165^\circ\text{C}$ , corresponding to the temperatures of phase transitions from opal-A to chert (see Yanchilina et al., 2020 and refs. therein). Four possible mixing trajectories between the diatoms and secondary endmembers are shown in blue and green. Hypothetical diagenetic silica includes equilibrium with pore water fluids ( $-3\text{‰}$  and  $-8\text{‰}$ ) at temperatures of  $30^\circ\text{C}$  and  $165^\circ\text{C}$ . The amount of diagenetic silica is shown with fractions between 0 and 1 (labeled as  $f$ ). The marine pore water fluids occupy the negative  $\delta^{18}\text{O}$  space and likely have positive  $\Delta^{17}\text{O}$ . The shown here range extends to extreme  $-10\text{‰}$  covering a wide range of pore water  $\delta^{18}\text{O}$  gradients. Possible hydrothermal fluids with positive  $\delta^{18}\text{O}$  values are shown with a green segment. Such fluids may be present in case of high-temperature ( $>250^\circ\text{C}$ ) alteration of seafloor basalts. The silica  $\delta^{18}\text{O}$ – $\Delta^{17}\text{O}$  are compiled from diatoms, seafloor-drilled cherts, subaerial Monterey, Fisco and Mishash formations as well as the Stevns Klint chert (Hayles et al., 2019; Ibarra et al., 2022; Sengupta et al., 2020; Sharp et al., 2016; Zakharov, Marin-Carbonne, et al., 2021) and this study. (b) The same diagram with enlarged scales in the range of our samples measured by secondary ion mass spectrometry (SIMS). The box plot margins are constructed from the 25th and 75th percentiles (marked Q1 and Q3, respectively) of the interquartile range of SIMS  $\delta^{18}\text{O}$  values. The median is shown as the vertical solid line within the box. The lengths of the whiskers are 1.5 of the interquartile range. The black dots are outliers. Two especially low  $\delta^{18}\text{O}$  outliers are shown with a dashed arrow in the sample 167-73-2-90-92. The bulk  $\delta^{18}\text{O}$ – $\Delta^{17}\text{O}$  of these samples are also plotted and color-coded by age (same as in panel (a)).

tive  $\Delta^{17}\text{O}$  values ( $+0.03$ ), thus corresponding to burial depths of 1–5 km, depending on the downward O-isotope gradients. We admit that the  $\Delta^{17}\text{O}$  of marine pore water fluids are underconstrained since the direct measurements of marine pore water fluids have not been extensively explored (however, see Galy, 2020). In addition, hydrothermal solutions may also contribute to chert-forming fluids. The subseafloor seawater-basalt reactions at  $\sim 350^\circ\text{C}$  produce fluids with positive  $\delta^{18}\text{O}$  and negative  $\Delta^{17}\text{O}$ . The range of such fluids is set by the water/rock ratios and basaltic equilibrium, where the most evolved compositions have  $\delta^{18}\text{O}$  of  $+4\text{‰}$  and  $\Delta^{17}\text{O} = -0.04\text{‰}$

(see Zakharov, Tanaka, et al., 2021), although the range of values is more limited compared to the marine pore water fluids (see Figure 11). The calculated compositional field covers published triple O-isotope data (including the data here) measured in cherts from the last 300 Ma (Hayles et al., 2019; Ibarra et al., 2022; Sengupta et al., 2020; Sharp et al., 2016; Zakharov, Marin-Carbonne, et al., 2021). Consequently, marine diagenesis could be the main reason for the observed scatter in the triple O-isotope diagram. Further, such compositional field is also in agreement with the majority of SIMS  $\delta^{18}\text{O}$  values plotted against the  $\Delta^{17}\text{O}$  measured in the same samples (Figure 11b). We however do not see any specific relationship between the range of  $\delta^{18}\text{O}$  SIMS values and the  $\Delta^{17}\text{O}$  of the cherts. Based on the triple O-isotope recrystallization path taken by silica, it is possible to assess the conditions of diagenesis, as silica recrystallized at high temperatures (100°C and higher) would exhibit  $\delta^{18}\text{O}$  and  $\Delta^{17}\text{O}$  values significantly lower than those cherts that were diagenetically recrystallized in cold conditions (30°C). Evidently, the heat flux through the oceanic crust during diagenesis must be one of the key parameters that defines the O-isotope composition of chert.

### 5.5. Tectonic Control of Marine Diagenesis

The age of the oceanic plate in such cases serves as the main factor determining the temperature of the last diagenetic transition. Other factors such as pore water fluids, sedimentation rates and chemical composition of sediment also play an important role in diagenesis determining the recrystallization timing and O-isotope of equilibrium fluids (Murata et al., 1977; Yanchilina et al., 2021). The cherts presented in this manuscript were accumulated on oceanic crust that was between 5 and 100 Ma at the time of original silica precipitation. The age of oceanic crust at the time of deposition can be derived from the age of cherts based on the biostratigraphy and accumulation rates (provided in the IODP reports; see <http://www-odp.tamu.edu/publications/>) and the age of the seafloor today (Müller et al., 2008). Given the difference in the ages of oceanic crust at the time of deposition, the cherts of this study were exposed to very different geothermal profiles ranging from 15 to 70°C/km, assuming an oceanic plate half space cooling model (e.g., Stein & Stein, 1992). To further explore the tectonic control on the oxygen isotope compositions of cherts we compiled the literature data from the seafloor-drilled 5–155 Ma cherts (Knauth & Epstein, 1975; Kolodny & Epstein, 1976; Yanchilina et al., 2021), and the ages of the underlying oceanic crust at the time of deposition. Based on depth of recovery, these deep-sea cherts largely depict moderate accumulation rates between 2 and 10 m/Ma.

The compiled data (Figure 12) shows a trend with increasing  $\delta^{18}\text{O}$  values of cherts that were accumulated on old oceanic plates. From the observed relationship it appears that deposition on old oceanic crust and low accumulation rates slow down the recrystallization of silica to crystalline cherts, which has been noticed before (Kolodny & Epstein, 1976). Cherts with  $\delta^{18}\text{O} > 35\text{‰}$  occur in sediments that accumulated at the rates below 10 m/Ma and were deposited on oceanic crust that is at least 45 Ma. Contrasting to these cherts are microquartz and other silica varieties deposited on a young and hot oceanic crust the Sea of Japan with an average age of 0–10 Ma and high accumulation rates of about 50 m/Ma (Ibarra et al., 2022; Yanchilina et al., 2020). In the latter case, recrystallization occurred at an early stage of marine diagenesis and was accompanied by high geothermal gradient, where recrystallized microcrystalline quartz has  $\delta^{18}\text{O}$  as low as 18‰ (Yanchilina et al., 2020). In summary, we find that the age of oceanic crust onto which chert is deposited plays a critical role in the oxygen isotope evolution of cherts during diagenesis.

These observations confirm our interpretations of marine diagenesis and its bearings on the triple O- and in-situ isotope compositions of cherts. Given the uncertainty of the seawater O-isotope composition and its temperature in the early geological periods (Jaffrés et al., 2007; Kasting et al., 2006; Robert & Chaussidon, 2006), the temperature of final microquartz recrystallization within the sediment column has to be considered. Such considerations have been recently presented by Tatzel et al. (2022) in a kinetically controlled model of chert diagenesis with incorporated changes in the heat flow through the geological history. Along with possible changes in  $\delta^{18}\text{O}$  of seawater, the  $\delta^{18}\text{O}$  trend recorded by Precambrian cherts may reflect the evolution of subseafloor diagenesis conditions, including the changes in geothermal gradients through the oceanic crust. Further, constraints are needed on the diagenetic transformations of silica that precipitated abiotically before the advent of the silica-secreting organisms at the end of Proterozoic eon.

## 6. Conclusions

In this study, we combined detailed mineralogical and isotope studies of seafloor-drilled cherts that have not been exposed subaerially. In addition, one sample from a subaerially exposed Cretaceous Mishash formation was studied. The bulk  $\delta^{18}\text{O}$  and triple O-isotope analyses, in situ  $\delta^{18}\text{O}$  and  $^{16}\text{OH}/^{16}\text{O}$  SIMS measurements as

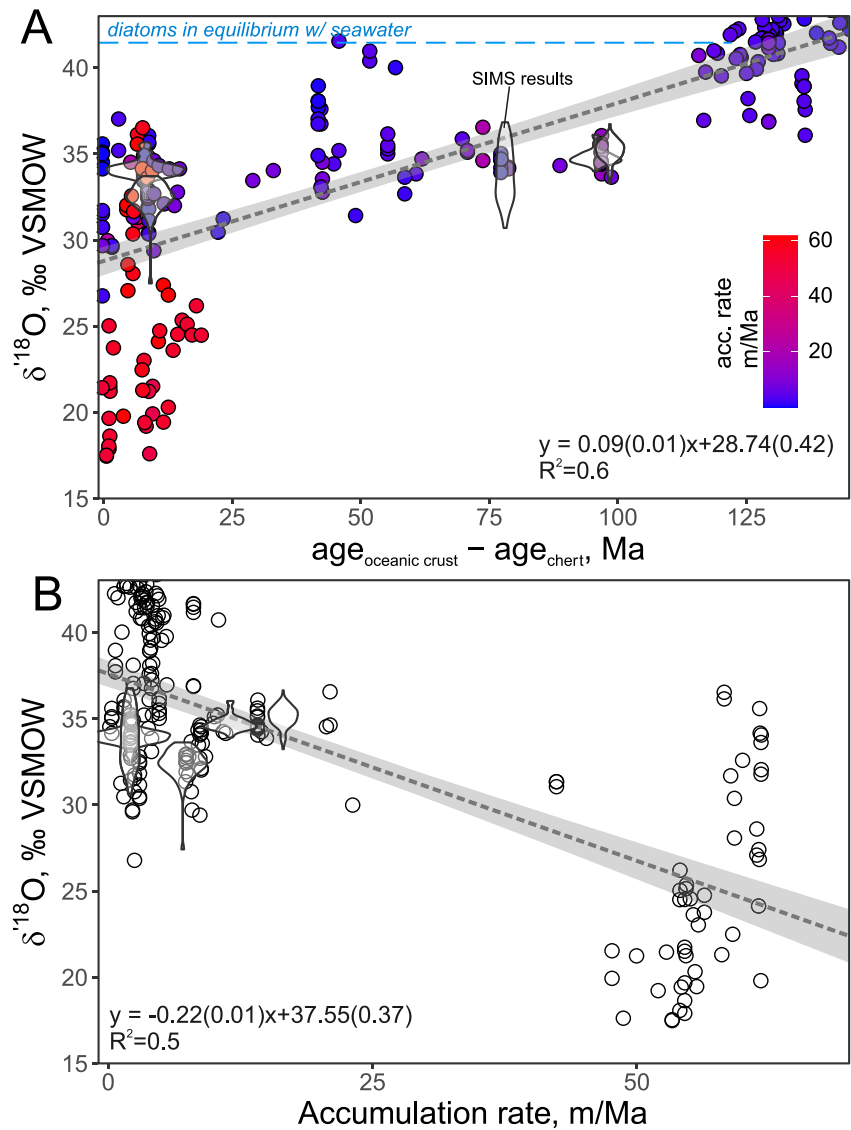


**Figure 12.** (a) The age of the oceanic crust at the time of deposition plotted against the  $\delta^{18}\text{O}$  values of silica extracted from modern seafloor, including cherts, opals and diatoms. The age of the crust at the time of deposition is calculated by subtracting the age of the cherts from today's age of oceanic crust ( $\text{age}_{\text{oceanic crust}} - \text{age}_{\text{chert}}$ ). The secondary ion mass spectrometry-results are shown at respective ages with violin diagrams. The data is color-coded by accumulation rates (depth of sediment divided by its age). (b) The accumulation rate is plotted against the  $\delta^{18}\text{O}$  value of the same silica samples. The linear regression between these two parameters and the  $\delta^{18}\text{O}$  highlights the dependence between heat flux through the sediment and the temperature regime during diagenesis. The equation and  $R^2$  value of the linear regression are shown. The uncertainties on the age of cherts vary on the scale of 1–20 Ma and are defined by the age models determined from microfossil chronostratigraphy originally detailed in the Ocean Drilling Program expedition reports.

well as the microprobe elemental mapping depict the isotope effects of marine diagenesis. The main findings are summarized below:

1. The investigated cherts have a range in  $\delta^{18}\text{O}$  between 29‰ and 38‰. The 1–2 mg bulk analyses yield limited heterogeneity of samples, mostly within 1‰. The detailed SIMS  $\delta^{18}\text{O}$  measurements show that most samples have a variability  $>1\%$  at the micrometer-scale, with a subset of samples having up to 6‰ of heterogeneity. In some samples, these  $\delta^{18}\text{O}$  heterogeneities correlate with petrographic observations, such as presence of filled radiolarian tests, and in others they are best explained by sub-10 $\mu$  (less than analytical spot) mineralogical silica varieties with different  $\delta^{18}\text{O}$  values. These heterogeneities point out to the effects of increased

- temperature during diagenesis and/or involvement pore water fluids with  $\delta^{18}\text{O}$  value lower than that of seawater that precipitate silica as low as 27.5‰ within the radiolarian tests.
- We suggest that SIMS  $\delta^{18}\text{O}$  measurements of recent cherts should be combined with the simultaneous measurements of  $^{16}\text{OH}/^{16}\text{O}$  ratio. The  $^{16}\text{OH}/^{16}\text{O}$  ratio serves as an indication of analytical bias and/or hydration water associated with analyses of hydrous opaline silica that yields high  $^{16}\text{OH}/^{16}\text{O}$  and low  $\delta^{18}\text{O}$  values. In our collection, this is relevant to one chert sample that contains aggregates of porcellanite, and to a museum species of MGL opal-CT used to test for analytical biases in hydrous silica with 5 wt.%  $\text{H}_2\text{O}$ .
  - The  $\delta^{18}\text{O}$ — $\Delta^{17}\text{O}$  values of the marine seafloor-drilled cherts plot near or under the silica-seawater equilibrium fractionation curve at temperatures between 25°C and 40°C. Since the changes in seawater O isotope composition are limited for the last 135 Myr, the systematics of the <135 Ma  $\delta^{18}\text{O}$ — $\Delta^{17}\text{O}$  chert values is best explained by sub-seafloor recrystallization at elevated temperatures and negative  $\delta^{18}\text{O}$  pore water fluids. Consequently, mixing between secondary and primary silica explains samples that do not plot on the equilibrium curve.
  - These considerations suggest that subseafloor temperatures are one of the main drivers for the final  $\delta^{18}\text{O}$ — $\Delta^{17}\text{O}$  values of the cherts. The age of the oceanic crust and hence overlying chert deposit at the time of deposition correlates with the  $\delta^{18}\text{O}$  of cherts. Together with high sedimentation rates, the high heat flux of young oceanic crust tends to promote crystallization of low  $\delta^{18}\text{O}$  cherts, while silica and cherts deposited on old oceanic crust with lower sedimentation rates have values close to the values of initial sediments (e.g., radiolaria and diatoms). Decreasing heat flux through the oceanic crust can potentially explain some of the observed long-term increase in cherts through geological time.

## Data Availability Statement

Data associated with this article is available via Zenodo repository <https://doi.org/10.5281/zenodo.7577323>.

## References

- Bauer, K. K., & Vennemann, T. W. (2014). Analytical methods for the measurement of hydrogen isotope composition and water content in clay minerals by TC/EA. *Chemical Geology*, 363, 229–240. <https://doi.org/10.1016/j.chemgeo.2013.10.039>
- Behl, R. J., Garrison, R. E., Iijima, I., Abed, A., & Garrison, R. (1994). The origin of chert in the Monterey Formation of California (USA). In *Siliceous, phosphatic and glauconitic sediments of the Tertiary and Mesozoic: Proceedings of the 29th International Geological Congress, Part C* (pp. 101–132).
- Behl, R. J., & Smith, B. M. (1992). Silicification of deep-sea sediments and the oxygen isotope composition of diagenetic siliceous rocks from the western Pacific Pigafetta and East Mariana Basins, Leg 1291. In *Proceedings of the Ocean Drilling Program, Scientific Results, College Station, TX (Ocean Drilling Program)* (pp. 81–117).
- Bernoulli, D., & Weissert, H. (2021). Oxygen isotopes in ophalcites: An ever-lasting controversy? *International Journal of Earth Sciences*, 110, 1–8. <https://doi.org/10.1007/s00531-020-01934-5>
- Cammack, J. N., Spicuzza, M., Cavosie, A., Van Kranendonk, M., Hickman, A., Kozdon, R., et al. (2018). SIMS microanalysis of the Strelley Pool Formation cherts and the implications for the secular-temporal oxygen-isotope trend of cherts. *Precambrian Research*, 304, 125–139. <https://doi.org/10.1016/j.precamres.2017.11.005>
- Catling, D. C., & Zahnle, K. J. (2020). The Archean atmosphere. *Science Advances*, 6(9), eaax1420. <https://doi.org/10.1126/sciadv.aax1420>
- Dodd, J. P., & Sharp, Z. D. (2010). A laser fluorination method for oxygen isotope analysis of biogenic silica and a new oxygen isotope calibration of modern diatoms in freshwater environments. *Geochimica et Cosmochimica Acta*, 74(4), 1381–1390. <https://doi.org/10.1016/j.gca.2009.11.023>
- Dodd, J. P., Sharp, Z. D., Fawcett, P. J., Brearley, A. J., & McCubbin, F. M. (2012). Rapid post-mortem maturation of diatom silica oxygen isotope values. *Geochemistry, Geophysics, Geosystems*, 13(9), Q09014. <https://doi.org/10.1029/2011gc004019>
- Epstein, S., Buchsbaum, R., Lowenstam, H., & Urey, H. C. (1951). Carbonate-water isotopic temperature scale. *The Geological Society of America Bulletin*, 62(4), 417–426. [https://doi.org/10.1130/0016-7606\(1951\)62\[417:citsj2.0.co;2](https://doi.org/10.1130/0016-7606(1951)62[417:citsj2.0.co;2)
- Galili, N., Shemesh, A., Yam, R., Brailovsky, I., Sela-Adler, M., Schuster, E. M., et al. (2019). The geologic history of seawater oxygen isotopes from marine iron oxides. *Science*, 365(6452), 469–473. <https://doi.org/10.1126/science.aaw9247>
- Galy, A. (2020). Triple oxygen and hydrogen isotopic variations of pore waters from the Middle Bengal Fran (IODP Exp. 354). In *Goldschmidt Abstracts Goldschmidt2020* (p. 780). Geochemical Society.
- Gieskes, J. M. (1981). Deep-sea drilling interstitial water studies: Implications for chemical alteration of the oceanic crust, layers I and II. In *The deep sea drilling project: A decade of progress* (Vol. 32, pp. 149–167).
- Gieskes, J. M., & Lawrence, J. R. (1981). Alteration of volcanic matter in deep sea sediments: Evidence from the chemical composition of interstitial waters from deep sea drilling cores. *Geochimica et Cosmochimica Acta*, 45(10), 1687–1703. [https://doi.org/10.1016/0016-7037\(81\)90004-1](https://doi.org/10.1016/0016-7037(81)90004-1)
- Graetsch, H., Flörke, O. W., & Miehe, G. (1985). The nature of water in chalcedony and opal-C from Brazilian agate geodes. *Physics and Chemistry of Minerals*, 12(5), 300–306. <https://doi.org/10.1007/bf00310343>
- Guo, M., Wostbrock, J. A. G., Planavsky, N. J., & Korenaga, J. (2022). Reconstructing seawater  $\delta^{18}\text{O}$  and  $\Delta^{17}\text{O}$  values with solid Earth system evolution. *Earth and Planetary Science Letters*, 592, 117637. <https://doi.org/10.1016/j.epsl.2022.117637>
- Hayles, J. A., Yeung, L. Y., Homann, M., Banerjee, A., Jiang, H., Shen, B., & Lee, C.-T. A. (2019). Three billion year secular evolution of the triple oxygen isotope composition of marine chert. *EarthArXiv*. <https://doi.org/10.31223/osf.io/n2p5q>
- Heck, P. R., Huberty, J. M., Kita, N. T., Ushikubo, T., Kozdon, R., & Valley, J. W. (2011). SIMS analyses of silicon and oxygen isotope ratios for quartz from Archean and Paleoproterozoic banded iron formations. *Geochimica et Cosmochimica Acta*, 75(20), 5879–5891. <https://doi.org/10.1016/j.gca.2011.07.023>

## Acknowledgments

JMC thanks the support of the European Research Council (ERC) under the European Union's Horizon program (STROMATA, Grant 759289). The authors are grateful to the ion probe group at CRPG, Nancy, particularly Nordine Bouden and Johan Villeneuve, and to Anne Sophie Bouvier and Florent Plane at the Swiss-SIMS laboratory, and Benita Putlitz at the Stable Isotope Laboratory at UNIL for their analytical help in this study. EMPA and SIMS analyses have been conducted at the Center for Advanced Surface Analysis, CASA: a joint facility between Université de Lausanne and École Polytechnique Fédérale de Lausanne (EPFL). Thanks to Maria Margarita Ariza Acero for help with the Raman determination of MGL opal-CT. The authors gratefully thank Yehoshua Kolodny and Marc Chaussidon for providing the samples for this study. Two anonymous reviewers are acknowledged for their constructive comments and suggestions. We thank the handling editor Adina Paytan. We also thank Nicole Russo for the assistance in the early stages of the project.

- Herwartz, D., Pack, A., & Nagel, T. J. (2021). A CO<sub>2</sub> greenhouse efficiently warmed the early Earth and decreased seawater <sup>18</sup>O/<sup>16</sup>O before the onset of plate tectonics. *PNAS*, *118*, e2023617118. <https://doi.org/10.1073/pnas.2023617118>
- Hinman, N. W. (1998). Sequences of silica phase transitions: Effects of Na, Mg, K, Al, and Fe ions. *Marine Geology*, *147*(1–4), 13–24. [https://doi.org/10.1016/s0025-3227\(98\)00002-4](https://doi.org/10.1016/s0025-3227(98)00002-4)
- Ibarra, D. E., Yanchilina, A. G., Lloyd, M. K., Methner, K. A., Chamberlain, C. P., Yam, R., et al. (2022). Triple oxygen isotope systematics of diagenetic recrystallization of diatom opal-A to opal-CT to microquartz in deep sea sediments. *Geochimica et Cosmochimica Acta*, *320*, 304–323. <https://doi.org/10.1016/j.gca.2021.11.027>
- Jaffrés, J. B. D., Shields, G. A., & Wallmann, K. (2007). The oxygen isotope evolution of seawater: A critical review of a long-standing controversy and an improved geological water cycle model for the past 3.4 billion years. *Earth-Science Reviews*, *83*(1–2), 83–122. <https://doi.org/10.1016/j.earscirev.2007.04.002>
- Kanzaki, Y., & Bindeman, I. N. (2022). A possibility of <sup>18</sup>O-depleted oceans in the Precambrian inferred from triple oxygen isotope of shales and oceanic crust. *Chemical Geology*, *604*, 120944. <https://doi.org/10.1016/j.chemgeo.2022.120944>
- Kasting, J. F., Howard, M. T., Wallmann, K., Veizer, J., Shields, G., & Jaffrés, J. (2006). Paleoclimates, ocean depth, and the oxygen isotopic composition of seawater. *Earth and Planetary Science Letters*, *252*(1–2), 82–93. <https://doi.org/10.1016/j.epsl.2006.09.029>
- Knauth, P. L., & Epstein, S. (1975). Hydrogen and oxygen isotope ratios in silica from the JOIDES deep sea drilling project. *Earth and Planetary Science Letters*, *25*, 1–10. [https://doi.org/10.1016/0012-821x\(75\)90204-6](https://doi.org/10.1016/0012-821x(75)90204-6)
- Knauth, P. L., & Epstein, S. (1976). Hydrogen and oxygen isotope ratios in nodular and bedded cherts. *Geochimica et Cosmochimica Acta*, *40*(9), 1095–1108. [https://doi.org/10.1016/0016-7037\(76\)90051-x](https://doi.org/10.1016/0016-7037(76)90051-x)
- Knauth, P. L., & Lowe, D. R. (1978). Oxygen isotope geochemistry of cherts from the Onverwacht Group (3.4 billion years), Transvaal, South Africa, with implications for secular variations in the isotopic composition of cherts. *Earth and Planetary Science Letters*, *41*(2), 209–222. [https://doi.org/10.1016/0012-821x\(78\)90011-0](https://doi.org/10.1016/0012-821x(78)90011-0)
- Kolodny, Y. (1969). Petrology of siliceous rocks in the Mishash Formation (Negev, Israel). *Journal of Sedimentary Research*, *39*, 166–175.
- Kolodny, Y., & Chaussidon, M. (2004). Boron isotopes in DSDP cherts: Fractionation and diagenesis. In *The Geochemical Society Special Publications* (pp. 1–14). Elsevier.
- Kolodny, Y., Chaussidon, M., & Katz, A. (2005). Geochemistry of a chert breccia. *Geochimica et Cosmochimica Acta*, *69*(2), 427–439. <https://doi.org/10.1016/j.gca.2004.07.010>
- Kolodny, Y., & Epstein, S. (1976). Stable isotope geochemistry of deep sea cherts. *Geochimica et Cosmochimica Acta*, *40*(10), 1195–1209. [https://doi.org/10.1016/0016-7037\(76\)90155-1](https://doi.org/10.1016/0016-7037(76)90155-1)
- Kolodny, Y., Taraboulos, A., & Frieslander, U. (1980). Participation of fresh water in chert diagenesis: Evidence from oxygen isotopes and boron  $\alpha$ -track mapping. *Sedimentology*, *27*(3), 305–316. <https://doi.org/10.1111/j.1365-3091.1980.tb01180.x>
- Lancelot, Y. (1973). Chert and silica diagenesis in sediments from the central Pacific. In E. L. Winterer, J. I. Ewing, R. G. Douglas, R. D. Jarrard, Y. Lancelot, R. M. Moberly, et al. (Eds.), *Initial reports of the deep sea drilling project* (Vol. 17, pp. 377–405). U.S. Government Printing Office.
- Lawrence, J. R., & Gieskes, J. M. (1981). Constraints on water transport and alteration in the oceanic crust from the isotopic composition of pore water. *Journal of Geophysical Research*, *86*(B9), 7924–7934. <https://doi.org/10.1029/jb086ib09p07924>
- Lawrence, J. R., Gieskes, J. M., & Broecker, W. S. (1975). Oxygen isotope and cation composition of DSDP pore waters and the alteration of Layer II basalts. *Earth and Planetary Science Letters*, *27*, 1–10. [https://doi.org/10.1016/0012-821x\(75\)90154-5](https://doi.org/10.1016/0012-821x(75)90154-5)
- Leng, M. J., & Barker, P. A. (2006). A review of the oxygen isotope composition of lacustrine diatom silica for palaeoclimate reconstruction. *Earth-Science Reviews*, *75*(1–4), 5–27. <https://doi.org/10.1016/j.earscirev.2005.10.001>
- Levin, N. E., Raub, T. D., Dauphas, N., & Eiler, J. M. (2014). Triple oxygen isotope variations in sedimentary rocks. *Geochimica et Cosmochimica Acta*, *139*, 173–189. <https://doi.org/10.1016/j.gca.2014.04.034>
- Liljestrand, F. L., Hania, A., Giordano, M., & Johnston, D. T. (2021). Calibrating the triple oxygen isotope signature of cultured diatoms. *Limnology & Oceanography*, *66*(12), 4254–4266. <https://doi.org/10.1002/lno.11958>
- Liljestrand, F. L., Knoll, A. H., Tosca, N. J., Cohen, P. A., Macdonald, F. A., Peng, Y., & Johnston, D. T. (2020). The triple oxygen isotope composition of Precambrian chert. *Earth and Planetary Science Letters*, *537*, 116167. <https://doi.org/10.1016/j.epsl.2020.116167>
- Lisiecki, L. E., & Raymo, M. E. (2005). A Pliocene-Pleistocene stack of 57 globally distributed benthic  $\delta^{18}\text{O}$  records. *Paleoceanography*, *20*(1), PA1003. <https://doi.org/10.1029/2004pa001071>
- Lowe, D. R., Ibarra, D. E., Drabon, N., & Chamberlain, C. P. (2020). Constraints on surface temperature 3.4 billion years ago based on triple oxygen isotopes of cherts from the Barberton Greenstone Belt, South Africa, and the problem of sample selection. *American Journal of Science*, *320*(9), 790–814. <https://doi.org/10.2475/11.2020.02>
- Marin, J., Chaussidon, M., & Robert, F. (2010). Microscale oxygen isotope variations in 1.9 Ga Gunflint cherts: Assessments of diagenesis effects and implications for oceanic paleotemperature reconstructions. *Geochimica et Cosmochimica Acta*, *74*(1), 116–130. <https://doi.org/10.1016/j.gca.2009.09.016>
- Marin-Carbonne, J., Faure, F., Chaussidon, M., Jacob, D., & Robert, F. (2013). A petrographic and isotopic criterion of the state of preservation of Precambrian cherts based on the characterization of the quartz veins. *Precambrian Research*, *231*, 290–300. <https://doi.org/10.1016/j.precamres.2013.03.019>
- Marin-Carbonne, J., Robert, F., & Chaussidon, M. (2014). The silicon and oxygen isotope compositions of Precambrian cherts: A record of oceanic paleo-temperatures? *Precambrian Research*, *247*, 223–234. <https://doi.org/10.1016/j.precamres.2014.03.016>
- Matheny, R. K., & Knauth, P. L. (1993). New isotopic temperature estimates for early silica diagenesis in bedded cherts. *Geology*, *21*(6), 519–522. [https://doi.org/10.1130/0091-7613\(1993\)021<0519:nitefe>2.3.co;2](https://doi.org/10.1130/0091-7613(1993)021<0519:nitefe>2.3.co;2)
- McGunnigle, J. P., Cano, E. J., Sharp, Z. D., Muehlenbachs, K., Cole, D., Hardman, M. F., et al. (2022). Triple oxygen isotope evidence for a hot Archean ocean. *Geology*, *50*(9), 991–995. <https://doi.org/10.1130/G50230.1>
- Miller, M. F., Pack, A., Bindeman, I. N., & Greenwood, R. C. (2020). Standardizing the reporting of  $\Delta^{17}\text{O}$  data from high precision oxygen triple-isotope ratio measurements of silicate rocks and minerals. *Chemical Geology*, *532*, 119332. <https://doi.org/10.1016/j.chemgeo.2019.119332>
- Muehlenbachs, K. (1998). The oxygen isotopic composition of the oceans, sediments and the seafloor. *Chemical Geology*, *145*(3–4), 263–273. [https://doi.org/10.1016/s0009-2541\(97\)00147-2](https://doi.org/10.1016/s0009-2541(97)00147-2)
- Müller, R. D., Sdrolias, M., Gaina, C., & Roest, W. R. (2008). Age, spreading rates, and spreading asymmetry of the world's ocean crust. *Geochemistry, Geophysics, Geosystems*, *9*(4), Q04006. <https://doi.org/10.1029/2007gc001743>
- Murata, K. J., Friedman, I., & Gleason, J. D. (1977). Oxygen isotope relations between diagenetic silica minerals in Monterey Shale, Temblor Range, California. *American Journal of Science*, *277*(3), 259–272. <https://doi.org/10.2475/ajs.277.3.259>

- Oster, J. L., Kitajima, K., Valley, J. W., Rogers, B., & Maher, K. (2017). An evaluation of paired  $\delta^{18}\text{O}$  and ( $^{234}\text{U}/^{238}\text{U}$ )<sub>0</sub> in opal as a tool for paleoclimate reconstruction in semi-arid environments. *Chemical Geology*, 449, 236–252. <https://doi.org/10.1016/j.chemgeo.2016.12.009>
- Pack, A., & Herwartz, D. (2014). The triple oxygen isotope composition of the Earth mantle and understanding  $\Delta^{17}\text{O}$  variations in terrestrial rocks and minerals. *Earth and Planetary Science Letters*, 390, 138–145. <https://doi.org/10.1016/j.epsl.2014.01.017>
- Pack, A., Tanaka, R., Hering, M., Sengupta, S., Peters, S., & Nakamura, E. (2016). The oxygen isotope composition of San Carlos olivine on the VSMOW2-SLAP2 scale: San Carlos olivine on the VSMOW2-SLAP2 scale. *Rapid Communications in Mass Spectrometry*, 30, 1495–1504. <https://doi.org/10.1002/rcm.7582>
- Perry, E. C., Jr., & Tan, F. (1972). Significance of oxygen and carbon isotope variations in early Precambrian cherts and carbonate rocks of southern Africa. *The Geological Society of America Bulletin*, 83(3), 647–664. [https://doi.org/10.1130/0016-7606\(1972\)83\[647:sooaci\]2.0.co;2](https://doi.org/10.1130/0016-7606(1972)83[647:sooaci]2.0.co;2)
- Qi, H., Coplen, T. B., Gehre, M., Vennemann, T. W., Brand, W. A., Geilmann, H., et al. (2017). New biotite and muscovite isotopic reference materials, USGS57 and USGS58, for  $\delta^2\text{H}$  measurements—A replacement for NBS 30. *Chemical Geology*, 467, 89–99. <https://doi.org/10.1016/j.chemgeo.2017.07.027>
- Raymo, M. E., Kozdon, R., Evans, D., Lisiecki, L., & Ford, H. L. (2018). The accuracy of mid-Pliocene  $\delta^{18}\text{O}$ -based ice volume and sea level reconstructions. *Earth-Science Reviews*, 177, 291–302. <https://doi.org/10.1016/j.earscirev.2017.11.022>
- Robert, F., & Chaussidon, M. (2006). A palaeotemperature curve for the Precambrian oceans based on silicon isotopes in cherts. *Nature*, 443(7114), 969–972. <https://doi.org/10.1038/nature05239>
- Savin, S. M., & Epstein, S. (1970). The oxygen and hydrogen isotope geochemistry of clay minerals. *Geochimica et Cosmochimica Acta*, 34(1), 25–42. [https://doi.org/10.1016/0016-7037\(70\)90149-3](https://doi.org/10.1016/0016-7037(70)90149-3)
- Sengupta, S., & Pack, A. (2018). Triple oxygen isotope mass balance for the Earth's oceans with application to Archean cherts. *Chemical Geology*, 495, 18–26. <https://doi.org/10.1016/j.chemgeo.2018.07.012>
- Sengupta, S., Peters, S. T. M., Reitner, J., Duda, J.-P., & Pack, A. (2020). Triple oxygen isotopes of cherts through time. *Chemical Geology*, 554, 119789. <https://doi.org/10.1016/j.chemgeo.2020.119789>
- Sharp, Z. D., Gibbons, J. A., Maltsev, O., Atudorei, V., Pack, A., Sengupta, S., et al. (2016). A calibration of the triple oxygen isotope fractionation in the  $\text{SiO}_2\text{-H}_2\text{O}$  system and applications to natural samples. *Geochimica et Cosmochimica Acta*, 186, 105–119. <https://doi.org/10.1016/j.gca.2016.04.047>
- Shemesh, A., Charles, C. D., & Fairbanks, R. G. (1992). Oxygen isotopes in biogenic silica: Global changes in ocean temperature and isotopic composition. *Science*, 256(5062), 1434–1436. <https://doi.org/10.1126/science.256.5062.1434>
- Stefurak, E. J., Fischer, W. W., & Lowe, D. R. (2015). Texture-specific Si isotope variations in Barberton Greenstone Belt cherts record low temperature fractionations in early Archean seawater. *Geochimica et Cosmochimica Acta*, 150, 26–52. <https://doi.org/10.1016/j.gca.2014.11.014>
- Stein, C. A., & Stein, S. (1992). A model for the global variation in oceanic depth and heat flow with lithospheric age. *Nature*, 359(6391), 123–129. <https://doi.org/10.1038/359123a0>
- Tatzel, M., Frings, P. J., Oelze, M., Herwartz, D., Lünsdorf, N. K., & Wiedenbeck, M. (2022). Chert oxygen isotope ratios are driven by Earth's thermal evolution. *Proceedings of the National Academy of Sciences*, 119(51), e2213076119. <https://doi.org/10.1073/pnas.2213076119>
- Taylor, H. P., & Epstein, S. (1962). Relationship between  $\text{O}^{18}/\text{O}^{16}$  ratios in coexisting minerals of igneous and metamorphic rocks: Part 1: Principles and experimental results. *GSA Bulletin*, 73, 461–480. [https://doi.org/10.1130/0016-7606\(1962\)73\[461:RBORIC\]2.0.CO;2](https://doi.org/10.1130/0016-7606(1962)73[461:RBORIC]2.0.CO;2)
- Veizer, J., Hoefs, J., Lowe, D. R., & Thurston, P. C. (1989). Geochemistry of Precambrian carbonates: II. Archean greenstone belts and Archean sea water. *Geochimica et Cosmochimica Acta*, 53(4), 859–871. [https://doi.org/10.1016/0016-7037\(89\)90031-8](https://doi.org/10.1016/0016-7037(89)90031-8)
- Williams, L. A., & Crerar, D. A. (1985). Silica diagenesis; II, General mechanisms. *Journal of Sedimentary Research*, 55, 312–321. <https://doi.org/10.1306/212F86B1-2B24-11D7-8648000102C1865D>
- Williams, L. A., Parks, G. A., & Crerar, D. A. (1985). Silica diagenesis; I, Solubility controls. *Journal of Sedimentary Research*, 55, 301–311. <https://doi.org/10.1306/212F86AC-2B24-11D7-8648000102C1865D>
- Westbrock, J. A. G., Cano, E. J., & Sharp, Z. D. (2020). An internally consistent triple oxygen isotope calibration of standards for silicates, carbonates and air relative to VSMOW2 and SLAP2. *Chemical Geology*, 533, 119432. <https://doi.org/10.1016/j.chemgeo.2019.119432>
- Westbrock, J. A. G., & Sharp, Z. D. (2021). Triple oxygen isotopes in silica–water and carbonate–water systems. *Reviews in Mineralogy and Geochemistry*, 86(1), 367–400. <https://doi.org/10.2138/rmg.2021.86.11>
- Westbrock, J. A. G., Sharp, Z. D., Sanchez-Yanez, C., Reich, M., van den Heuvel, D. B., & Benning, L. G. (2018). Calibration and application of silica–water triple oxygen isotope thermometry to geothermal systems in Iceland and Chile. *Geochimica et Cosmochimica Acta*, 234, 84–97. <https://doi.org/10.1016/j.gca.2018.05.007>
- Yanchilina, A. G., Yam, R., Kolodny, Y., & Shemesh, A. (2020). From diatom opal-A  $\delta^{18}\text{O}$  to chert  $\delta^{18}\text{O}$  in deep sea sediments. *Geochimica et Cosmochimica Acta*, 268, 368–382. <https://doi.org/10.1016/j.gca.2019.10.018>
- Yanchilina, A. G., Yam, R., & Shemesh, A. (2021). The effect of sediment lithology on oxygen isotope composition and phase transformation of marine biogenic opal. *Chemical Geology*, 570, 120175. <https://doi.org/10.1016/j.chemgeo.2021.120175>
- Zachos, J., Pagani, M., Sloan, L., Thomas, E., & Billups, K. (2001). Trends, rhythms, and aberrations in global climate 65 Ma to present. *Science*, 292(5517), 686–693. <https://doi.org/10.1126/science.1059412>
- Zakharov, D. O., Marin-Carbonne, J., Alleon, J., & Bindeman, I. N. (2021). Triple oxygen isotope trend recorded by Precambrian cherts: A perspective from combined bulk and in situ secondary ion probe measurements. *Reviews in Mineralogy and Geochemistry*, 86(1), 323–365. <https://doi.org/10.2138/rmg.2021.86.10>
- Zakharov, D. O., Tanaka, R., Butterfield, D. A., & Nakamura, E. (2021). A new insight into seawater–basalt exchange reactions based on combined  $\delta^{18}\text{O}$ – $\Delta^{17}\text{O}$ – $^{87}\text{Sr}/^{86}\text{Sr}$  values of hydrothermal fluids from the axial Seamount volcano, Pacific ocean. *Frontiers of Earth Science*, 9, 691699. <https://doi.org/10.3389/feart.2021.691699>